Effect of bridge abutment length on turbulence structure and flow through the opening

Chua, Ken Vui; Fraga, Bruno; Stoesser, Thorsten; Hong, Seunghoon; Sturm, Terry

DOI:
10.1061/(ASCE)HY.1943-7900.0001591

Document Version
Peer reviewed version

Citation for published version (Harvard):
Chua, KV, Fraga, B, Stoesser, T, Hong, S & Sturm, T 2019, 'Effect of bridge abutment length on turbulence structure and flow through the opening', *Journal of Hydraulic Engineering*, vol. 145, no. 6, 04019024. https://doi.org/10.1061/(ASCE)HY.1943-7900.0001591

The Effect of Bridge Abutment Length on the Turbulence Structure and the Flow Through the Opening

Ken Vui Chua[1], Bruño Fraga[2], Thorsten Stoesser, M. ASCE[3], Terry Sturm, F. ASCE[4], and Seung Ho Hong[5]

[1]Hydro-environmental Research Centre, School of Engineering, Cardiff University, The Parade, Cardiff, UK CF24 3AA. Email: chuakv@cardiff.ac.uk

[2]School of Engineering, University of Birmingham, Edgbaston, Birmingham, UK B15 2TT. Email: B.Fraga@bham.ac.uk

[3]Engineering Fluid Dynamics Research Centre, School of Civil, Environmental and Geomatic Engineering, University College London, Gower Street, London, UK WC1E 6BT. Email: t.stoesser@ucl.ac.uk

[5]Department of Civil and Environmental Engineering, West Virginia University, Morgantown, WV, US 26506. E-mail: sehong@mail.wvu.edu

[4]School of Civil and Environmental Engineering, Georgia Institute of Technology, Atlanta, GA, US 30332. E-mail: terry.sturm@ce.gatech.edu

ABSTRACT

The method of large eddy simulation (LES) is employed to investigate the flow and the turbulence structure around bridge abutments of different lengths placed in a compound, asymmetric channel. The simulations are faithful representations of large-scale physical model experiments which were conducted in the hydraulics laboratory at the Georgia Institute of Technology. The experiments are considered idealised hydraulic models of the Towaliga River bridge at Macon, Georgia, USA, consisting of flat horizontal floodplains on both sides of a parabolic main channel, two spill-through abutments with varying lengths (long-set back, LSB and short-set back, SSB)

and a bridge spanning across the abutments. In the LES a 'free flow' scenario is simulated where the water surface is not perturbed by the bridge at any point. The Reynolds number, based on the bulk velocity and hydraulic radius are 76,300 and 96,500 for LSB and SSB abutments respectively. Validation of the simulation results using data from the complementary experiment is presented and agreement is found to be reasonably good. Thorough comparison of various flow variables between LSB and SSB scenarios to highlight the effect of the flow contraction is carried out in terms of flow separation and instantaneous secondary flow, streamwise velocity, streamlines, streamtraces and turbulence structures. Further flow instability and vortex shedding generated in the shear layer downstream of the abutments are quantified by analysing timeseries of the instantaneous velocity in the form of probability density function, quadrant analysis and power density spectra.

INTRODUCTION

Bridge support structures cause flow contraction and the formation of scour around the bridge foundation that, according to the literature, may lead to bridge failure. During extreme flood events, the scale of the scouring process is magnified, leading to higher chance of bridge failure. Shirole and Holt (1991) collected data on about 1000 bridges for 30 years since the sixties and reported up to 60% of the bridge failures were due to scour at the bridge foundation. Data collected for the following 12 years on over 500 bridges has a similar outcome of 53% failure due to flood and scour (Wardhana and Hadipriono 2003). More recently, Lin et al. (2014) carried out a very detailed study on the scour type, scour depth and flow characteristics in 36 historically failed bridges. It was concluded that 64% of the bridge failures were caused by local scour. However, the accurate prediction of scour has always been a challenge for researchers and engineers.

Experimental work on scour formation around abutment-like structures has generally concentrated on deducing scour-prediction formulas by defining a few of the key parameters affecting scour such as the abutment length, flow depth, abutment shape, flow intensity and sediment characteristics(Melville 1992; Melville 1995). Laursen (1963) suggested that local abutment scour could be predicted as an amplification factor applied to a theoretical contraction scour depth. However,

later studies modified Laursen's approach and proposed that the amplification factor for abutment scour in compound channels should be applied on the basis of a discharge contraction ratio rather than a geometric contraction ratio (Sturm and Janjua 1994; Sturm 2006; Ettema et al. 2010). Hong et al. (2015) investigated three different water depths, including free surface, submerged orifice and overtopping flows, with the inclusion of a bridge structure and found that turbulent kinetic energy (TKE) near the bed could be related to the amplification factor used for scour prediction as regions of high TKE coincide with the scour location. Scour-prediction formulas are very useful to practical forecasting of the erosion around in-stream structures but they do not provide detailed understanding of the physical processes involved, especially as related to turbulence, flow separation, and flow contraction combined.

The scouring mechanism around large obstacles is well documented. Large-scale energetic coherent structures are induced by the presence of immersed bodies that contribute and magnify the shear stress and pressure fluctuations originating at the channel bed. As a result, solid particles are detached and entrained from the bottom sediment layer and a scour hole begins developing around the in-stream structure (Sumer and Fredsøe 2002; Fael et al. 2006). Koken and Constantinescu (2014) described the scour process around abutment-like structures in three main steps: (1) the acceleration of flow past the flank or edge of the abutment; (2) the horseshoe vortex (HV) structure forming because of the downflow and adverse pressure gradients present in the vicinity of the upstream side of the abutment; and (3) the vortical structures shed in the separated shear layer (SSL) forming in between the fast outer flow and the recirculation region behind the abutment. Koken and Constantinescu (2014) used detached eddy simulation (DES) to simulate a trapezoidal abutment with sloped sidewalls in a straight channel and found that when compared to simple vertical spur dikes/abutments (Paik and Sotiropoulos 2005; Koken and Constantinescu 2008b; Koken and Constantinescu 2008a; Koken 2011), the formation, dynamics and position of the large-scale coherent structures around the abutment are very different, mainly due to the reduced deceleration and smaller adverse pressure gradient of the incoming flow on the upstream face of the abutment. (Koken 2017) continued his previous work and added another spill-through abutment on the other

side of the channel to obtain insights on the generation of coherent structures in the contraction. A number of studies investigated the hydraulics of one-sided compound channels and generally reported a particular interest at the interface between the main channel and floodplain, where the secondary flow drives the lateral momentum transfer between the main channel and the floodplains, increasing the bed stress on them (Cater and Williams 2008; Kara et al. 2012; Xie et al. 2013).

Most of the aforementioned numerical studies that involve a free surface and large obstructions to the flow employed the so called rigid-lid assumption, in which a fixed (generally flat) surface or lid is used to represent the water surface. In the majority of the cases, the validity of the assumption can be justified by a low Froude number (i.e. Fr<0.5) (see (Rodi et al. 2013) for more discussion). Kara et al. (2015) performed LES to compare two different treatments of the free surface in a channel with side mounted abutment: rigid-lid and level-set method (LSM). They showed that the turbulence structure in the flow is strongly influenced by the water-surface deformation while highlighting the limitation of the rigid lid approximation and the requirement for more sophisticated approaches. Yue et al. (2005) carried out LES on turbulent flow of different flow depths over a fixed two-dimensional dune in which the free surface is computed using the LSM. The results suggested strong interaction between the free surface and near-bed flow structures in the shallower flow case, providing insights that the use of moving and deforming free surface is necessary especially in relative shallow water.

This study attempts to contribute to the design of resilient hydraulic structures by elucidating the complex flow mechanisms around bridge abutments in changing conditions. Large eddy simulations of the turbulent flow around bridge abutments of different lengths are performed, using the level-set method to predict the free surface deformation. The relatively high constriction to which the flow is subjected may produce fairly high local Froude numbers that prevent the rigid lid assumption. The simulations are an exact reproduction of the large-scale laboratory experiments of Hong et al. Hong et al. (2015) the data of which are used to validate the simulations. The computational domain consists of an asymmetrical compound geometry with a parabolic main channel in which two variable-length abutments with sloped sidewalls and rounded corners are placed. The

challenge of the present study from a numerical point of view relies on the concurrence of several factors: a) a numerical setup that solves the larger scales of turbulence; b) fluid-structure interaction, including important flow contraction; c) free-surface prediction; d) complex and realistic (compound and asymmetric) channel. To the authors' knowledge, such analysis has rarely been carried out in the past, less so with these factors combined. The present paper proceeds firstly to validate the large-eddy simulation with complementary experimental data. It then discusses the differences on the mean flow patterns between the two abutment configurations, focusing on the effect of increasing contraction on the extent of the recirculation vortices and the oscillation of the shear layer between this recirculation and the main channel flow. Thirdly, the results focus on the analysis of the coherent structures shed by the abutments, whose shapes, vorticity and periodicity are analysed by means of the Q-criterion and spectral analysis. The resulting data may contribute to the assessment of reduced-order models and the unveiling of relevant flow mechanisms.

NUMERICAL FRAMEWORK

The in-house HYDRO3D LES code is used to solve the filtered Navier-stokes equations for an unsteady, incompressible, viscous flow (Stoesser and Nikora 2008; Stoesser 2010; Bomminayuni and Stoesser 2011; Stoesser et al. 2015; Fraga et al. 2016; Fraga and Stoesser 2016; Liu et al. 2016; Ouro et al. 2017b). LES is an eddy-resolving technique in which the energetic portion of the flow is simulated directly and only the sub-grid scale turbulence is modelled (Stoesser 2014), and is therefore capable of explicitly predicting unsteadiness in flows of eningeering importance (Koken and Constantinescu 2009). The effects of the small-scale turbulence on the large eddies are calculated using the Wall-Adapting Local Eddy-viscosity (WALE) sub-grid scale model introduced by Nicoud and Ducros (1999). The diffusive terms are approximated by a fourth-order central difference scheme while convective fluxes in the momentum and level-set equations are approximated using a fifth-order weighted, essentially non-oscillatory (WENO) scheme. A fractional-step method is adopted with a Runge-Kutta predictor and the multigrid method is used to solve the Poisson pressure-correction equation.

The Immersed Boundary Method (IBM), which maps Eulerian velocities onto Lagrangian

point-based representations of non-fluid bodies in the flow, is used to define the geometries of the abutments and bridge. The accuracy of the IBM for fluid-structure interaction is provided by: a) use of high-order convection-diffusion schemes; b) Eulerian-Lagrangian interpolation through delta-functions (Ouro and Stoesser 2017; Ouro et al. 2017a; Ouro et al. 2017b); c) high mesh resolution near solid boundaries. The position of the free surface is tracked using the Level Set Method developed by Osher and Sethian (1988), which defines a sharp air-water interface across which the density and viscosity transition smoothly through a level set signed distance function, ϕ, which has zero value at the phase interface and is negative in air and positive in water. This method is formulated as:

$$\phi(x,t) < 0 \quad \text{if} \quad x \in \Omega_{gas} \tag{1}$$

$$\phi(x,t) = 0 \quad \text{if} \quad x \in \Gamma \tag{2}$$

$$\phi(x,t) > 0 \quad \text{if} \quad x \in \Omega_{liquid} \tag{3}$$

where Ω_{gas} and Ω_{liquid} represent the fluid domains for gas and liquid, respectively, and Γ is the interface. The LSM is proven successful in multiple two-phase flow studies (Sussman et al. 1994; Yue et al. 2006; Kang and Sotiropoulos 2012; McSherry et al. 2018).

LABORATORY EXPERIMENTS AND NUMERICAL SETUP

The computational setup shown in Fig. 1 replicates closely the physical experiments carried out at the Georgia Institute of Technology, US, similar to those presented in Hong et al. (2015). The physical model consists of a 24.4 m long steel flume of 4.26 m width and 0.76 m depth. It is an idealised hydraulic model of the Towaliga River bridge at Macon, Georgia which consists of flat horizontal floodplains on both sides of a main channel. Two spill-through abutments of depth 0.084 m, 2:1 slope and 0.636 m width with varying lengths are analysed in the large-eddy simulations. The shorter abutment (on the right floodplain) is the same length for both cases which extends to the edge of the main channel. At the left (downstream view) floodplain, two different abutment lengths, $0.41B_f$ and $0.77B_f$, are chosen - Long Setback (LSB) and Short Setback (SSB) cases respectively, where $B_f = 2.59m$ is the width of the left floodplain. The main channel is 0.96

m wide and extends streamwise along the whole length of the domain; it exhibits a parabolic cross-section with a maximum depth of 0.13 m. The bridge deck (0.292 m wide and 0.033 m tall) sits on top of the abutments and spans the full width of the channel. The numerical model duplicates the geometries of the physical model except for a shorter streamwise length, which was compensated by the use of a fully-developed flow inlet condition - explained in the paragraphs to follow. The length of the computational domain is 15 m and 21 m in LSB and SSB respectively. These domain lengths are chosen by running multiple attempts to make sure all large-scale recirculation and turbulence downstream of the abutments are captured and are not affected by the outflow boundary condition.

The conditions of the laboratory experiments are carefully replicated in the numerical simulations. The discharge for LSB and SSB cases is set to $0.085 m^3/s$ and $0.108 m^3/s$ respectively. In the experiment the water depth was controlled by a tailgate during the experiments to ensure a water depth of 20 cm at the deepest part of the main channel under the bridge, and this condition was ensured in the simulations. In such conditions, labelled as 'free flow scenario', the water surface is not perturbed by the bridge at any point. The resulting bulk velocities are $U_b = 0.24 m/s$ and $0.29 m/s$; the Reynolds numbers, based on the bulk velocity and four times the hydraulic radius (Kara et al. 2012), are $Re = 76,300$ and $96,500$; finally, the global Froude numbers, based on U_b and the average water depth D, are $Fr = 0.27$ and 0.32 for LSB and SSB cases respectively.

Fully developed turbulent inflow conditions are prescribed at the upstream boundary of the domain. This is achieved by running precursor simulations in the absence of abutments and employing periodic boundaries. Once the flow achieves full development (based on first and second-order statistics), the 3-D instantaneous flow field at one cross-section of the periodic channel is recorded for 10,000 time steps and then provided as the inflow of the LSB and SSB simulations. The precursor inflow velocity planes are recycled every 10,000 time steps, ensuring a continuous fully-developed turbulent inflow for the duration of the simulation. This procedure has the disadvantage of introducing periodicity in the turbulence field, which was judged not particularly relevant due to the fact that the area of interest is located at or dowmstream of the contraction,

where the interaction with the abutments substantially alters the flow. Convective boundary conditions are adopted at the outlet plane. No-slip boundary conditions are employed on the side walls and channel bed while the level set method is applied to track the position of the free surface. The initial free surface height, h is estimated based on the experimental measurements and is assumed flat at the start of the simulation. The abutments, bridge, and the parabolic channel boundaries are represented by a Lagrangian field of immersed boundaries.

Coarse and fine uniform numerical grids are generated for both scenarios. The coarse grid (or mesh) for the LSB case comprises 1500x426x80 grid points in the streamwise, spanwise and vertical directions, respectively, whereas the fine mesh doubles the resolution in all directions resulting in 3000x852x160 grid points. The total number of grid points for the LSB cases are 51M and 409M for coarse- and fine-mesh resolutions, respectively. The SSB case has the same mesh resolution as the LSB in both coarse- and fine-mesh simulations but requires a longer domain in the streamwise direction, resulting in 72M and 576M grid points, respectively. The number of CPU cores required for the coarse- and fine-grid simulations are 300 and 1000, respectively for both LSB and SSB cases. The coarse-grid simulations run for approx. 6 days while the fine-grid simulations take approx. 12 days to achieve sufficiently averaged flow statistics.

RESULTS AND DISCUSSION

Validation

Profiles of computed and measured time-averaged streamwise velocity at the locations described in Fig. 2 are plotted in Figs. 3 and 4 for LSB and SSB cases, respectively. The experimental velocities were measured with microADV probes; a detailed description of the ADV setup can be found in Hong (2012). The validation points are located at five cross-sections: `Up_toe(1)` and `down_toe(4)` at the upstream and downstream toes of the abutments respectively; `Up_bridge(2)` and `down_bridge(3)` at the upstream and downstream faces of the bridge respectively; and `down_further(5)`, located 0.15 m downstream of `down_toe`. The intersections between the aforementioned cross-sections (1)-(5) and the solid (for LSB) and dashed (for SSB) lines from Fig. 2 provide the locations at which the time-averaged velocity profiles (a)-(h) exhibited in Figs.

3 and 4 are extracted. In Figs. 3 and 4, dashed horizontal lines show the approximate water surface elevation at the corresponding location while solid horizontal lines represent the channel bed. The vertical coordinate z is scaled with the initial water depth h at the deepest point ($h = 0.2039$ m for LSB and $h = 0.2068$ m for SSB). Circles, dashed line and solid line represent the experimental, the coarse-mesh LES and the fine-mesh LES data, respectively. For brevity only the validation profiles at cross-sections 2, 3, and 4 are shown, the other two cross-sections are very similar in terms of the match between experimental and numerical data. Also, for brevity only the streamwise velocity validation is shown here, nevertheless LES-predicted spanwise and vertical velocity profiles were also compared with experimental data and the overall agreement is found to be very similar to what is reported in the following for the streamwise velocities.

The overall agreement between the experimental data and the LES results for the LSB case is remarkably good. The predicted velocities match the measured ones quite well, except at the 3-4 (h) profiles, which are located in the vicinity of the right abutment, where the simulations overestimate the streamwise velocity by approximately 50%. This is probably due to slight differences in the right abutment's geometry or slight location differences between experiments and simulations. The numerical results obtained with the fine mesh (solid line) generally match better the experimental measurements in all profiles except (a), where they tend to overestimate the velocities obtained in the laboratory. The fine-mesh LES performs very well in predicting the near-bed streamwise velocity due to its higher resolution near the bed.

Fig. 4 allows quantitative comparisons of the simulated time-averaged streamwise velocity profiles with the experimental data for the SSB case. The agreement between the coarse and fine simulations is again convincing particularly in the main channel. Both grids seem to capture well the details of the flow when subjected to a significant contraction. As with the LSB setup, the velocities at some of the (h) profiles are overestimated by the LES in the vicinity of the right abutment. There are no significant differences between the results for two mesh resolutions for the most part, with the fine mesh slightly more accurate in the near-bed region, whereas the coarse LES arguably shows somewhat better agreement at the upper half of some profiles at cross-sections

2 and 3. Profiles 3-4 (a) show significant discrepancies between both grid resolutions, probably related to the fact that this location is under the influence of the shear layer produced by the left abutment, and slight changes in its prediction have a great effect on the local velocities. It also appears that the LES has achieved a reasonable grid convergence (the results of both meshes do not offer significant differences). The succeeding plots in this paper are based on the data set obtained from the fine-mesh simulations.

Figs. 5 and 6 present LES-computed water surface elevations together with experimental measurement data at 15 locations along cross-sections 2, 3 and 4. The numerical data points are are the level set $\phi = 0$, which represents the relatively sharp boundary between the two fluids (water and air). Overall, both LSB and SSB simulations provide a reasonable prediction of the water surface elevation. The free surface is close to horizontal with a very gradual slope towards the right abutment in the LSB case. The acceleration due to significant flow contraction of the SSB case results in a water surface deformation, in the form of a depression near the abutments. The depression is slightly more significant in the LES profile than in the experimental point gauge measurements.

Flow Separation

The instantaneous (a) and time-averaged (b) streamwise velocity contours for LSB and SSB in a horizontal plane located 15 cm above the deepest point (2 cm above the floodplain bed) are presented in Figs. 7 and 8. The dashed lines represent the zero streamwise velocity, hence highlighting the flow separation and recirculation downstream of the abutments. Several relevant flow phenomena can be observed in these plots. Firstly, the effect of contraction: the flow accelerates towards the abutments due to continuity, reaching at the contraction $2U_b$ in the LSB case and $2.5U_b$ in the SSB case. Secondly, the abutment induces flow separation and a significant recirculation bubble downstream of the abutments forms; the recirculation extends x/b=1.82 for LSB and x/b=2.39 for SSB (see Fig. 9 for details) cases, respectively. Thirdly, the velocity contours reflect rather clearly the banks of the main channel in the form of a velocity drop (white line), indicating the impact of the secondary motion at the channel-floodplain interface on the streamwise velocity. Regarding the differences between the time-averaged and instantaneous streamwise velocity

fields, Figs. 7 and 8 rather nicely illustrate the distinctive scale of the medium-scale instantaneous eddies versus the large-scale structures of the mean flow. The meandering motion induced by the contraction on the flow in the main channel is particularly remarkable in the SSB case. Fig. 8a) suggests that these oscillations at the main channel interface produce periodical ejections towards the floodplains, particularly the left one.

2D (left) and 3D (right) streamlines are presented in Fig. 9 for LSB (top) and SSB (bottom) cases. The two-dimensional flow field is extracted at a plane 15 cm above the deepest point of the main channel; the 3D streamlines are colour-coded by the time-averaged streamwise velocity $< u >$. The flow separation is visualised and quantified and several recirculation zones occur. The first one is located upstream of the abutments a result of the blockage they exert on the oncoming flow. Small corner vortices are formed at the junction between the upstream toe and the side walls, which are similar in size for both setups. The flow past the abutments is dominated by large recirculation cells featuring counter-clockwise rotating vortices in both cases. The left abutment's recirculation of the SSB case extends much further downstream and reaches $x/b = 2.39$ before the flow reattaches to the side wall, whereas for LSB (shorter left abutment) the flow reattaches at approx. $x/b = 1.82$. Comparing both cases, the ratio between the lengths of the recirculation bubbles $\frac{X_{SSB}}{X_{LSB}} = 1.3$ is significantly smaller than the ratio between the left abutments' lengths $\frac{0.77B_f}{0.41B_f} = 1.9$, but rather similar to the ratio between the maximum velocities $\frac{U_{SSB}}{U_{LSB}} = 1.25$. These counter-clockwise eddies are complemented by corner vortices (labeled CV1 and CV2) at the downstream junction of the left abutment which rotate in the clockwise direction. Interestingly, while CV1 covers the whole length of the abutment, CV2 is more constrained towards the side wall, which may be explained by the dominance of the main recirculation cell. The larger contraction ratio of the SSB case causes the flow to veer more substantially towards the right side of the main channel; the streamlines are diverted almost immediately after the bridge opening onto the right floodplain and flow reattachment takes place at $x/b = 0.765$. For the LSB case, the main channel is not deflected towards the right bank and hence the reattachment does not occur until $x/b = 0.884$, allowing a slightly larger and more defined recirculation eddy behind the right abut-

ment in comparison with the rather short compressed recirculation zone of the LSB case. Figs. 9c and 9d highlight again the difference in extent of recirculation between cases and also visualise the significant flow acceleration that takes place through the opening and high velocities are sustained until the end of the respective recirculation zones. The similarities of the vortical structures' shapes and sizes between the 2D and 3D figures demonstrate that the flow is predominantly two-dimensional in the shallow floodplains.

Instantaneous Secondary Flow

The previous section discussed the main features of the time-averaged flow separation and recirculation bubbles behind the abutments. However, in the context of a turbulent flow, the shape and size of these coherent structures is subjected to the interaction with transitory structures which provoke oscillations and meandering (see Fig. 8a), resulting in increased turbulence. Of particular interest is the region behind the abutments which is where three turbulence structures interact: a) the shear layer between the recirculation zones and the main flow, b) the vortices shed from the abutments' tip, c) the transition between the main channel and the floodplain.

Fig. 10 presents isosurfaces of the Q-criterion together with vorticity contours in selected cross-sections. The Q-criterion (e.g. (Dubief and Delcayre 2000)) is defined as:

$$Q = \frac{1}{2}(|\Omega| - |S|) \tag{4}$$

in which $|\Omega|$ and $|S|$ are the rotation and strain rates, respectively:

$$|\Omega| = \sum_{i,j=1}^{3} \left[\frac{1}{2} \left(\frac{\partial u_i}{\partial x_j} - \frac{\partial u_j}{\partial x_i} \right) \right]^2 \tag{5}$$

$$|S| = \sum_{i,j=1}^{3} \left[\frac{1}{2} \left(\frac{\partial u_i}{\partial x_j} + \frac{\partial u_j}{\partial x_i} \right) \right]^2 \tag{6}$$

where u_i and u_j are instantaneous velocity components. Positive isosurfaces of Q isolate areas where the strength of rotation overcomes the strain, thus visualising rotation in the form of vortex tubes. The Q-criterion isosurfaces are colour-coded with the streamwise vorticity ω_x, which mea-

sures the rotation intensity around the streamwise x axis, hence on the YZ cross-sectional plane. Positive streamwise vorticity (red) corresponds to clockwise rotation while blue represents anti-clockwise motion. The Q-criterion isosurfaces are complemented with three cross-sectional slices of the ω_x field in between and downstream of the abutments to help understand the secondary motion. The vortex tubes labelled SSL are shed from the tip of the abutments and then convected downstream along the shear layer formed between the accelerated flow through the opening and the recirculating, low-momentum zones of the floodplains and downstream of the abutments. The NV label identifies 'necklace vortices', which can be found near the abutments as an offset of the SSLs towards the main channel. NVs form before approaching the abutments, more noticeably for the right abutment in both cases. NVs are better defined and exhibit a more consistent streamwise vorticity colouring than SSLs, i.e. they portray their stable rotating motion (clockwise by the left abutment and anti-clockwise by the right one). In both LSB and SSB cases, a long patch of interface vortices (IV) appear as a result of the momentum exchange between the right edge of the main channel and the floodplain; starting upstream of the right abutment as the flow is forced into the main channel. The same flow mechanism produces a very well-defined IV at the interface between the main channel and the left floodplain but only for the SSB case (Fig. 10b). In the LSB case (Fig. 10a), no IV is found on the left side of the main channel, highlighting the differences between the two contraction ratios. Interestingly, a counter-rotating vortex pair near the water surface labelled as SV can only be found in the LSB results. The SV pair consists of both short clockwise and long anti-clockwise rotating vortices side by side near the surface and off centre towards the left of the main channel. When visualising simultaneously instantaneous velocity streamlines (not shown for clarity and brevity), the SV pair forms where the surface flow coming from the left and right floodplains meet over the main channel.

Fig. 11 presents three-dimensional views of the water surface ($\phi = 0$ level-set isosurface) at an instant in time for the LSB and SSB cases, respectively. The vertical axis is exaggerated by a factor of 10 to highlight better the features of the water surface deformations. The coherent structures described in Fig. 10 have a clear signature at the free surface; regularly recurring dips in the water

surface are the low-pressure core of the shear layer vortices in both cases, although the dips are more prominent in the SSB geometry due to a stronger shear layer and vortices. The effect of the SV on the free surface of the LSB setup is very noticeable and it appears in Fig. 11a) as a persistent bulging line.

Shear Layer Oscillation and Vortex Shedding

With the aim of quantifying the oscillations and the vorticity generated in the shear layer behind the abutments for different contraction ratios, several timeseries' of velocity are recorded at selected sampling points for both LSB and SSB cases over a relatively long period of simulation time (approx. 150 seconds which corresponds to 2-3 flow through times) and at a frequency of 500Hz. The time-series obtained are analysed using: probability density function, quadrant analysis and power density spectra, and the data are related to the physics of the instantaneous flow. The probability density function is calculated by first, sorting the recorded signal of streamwise velocity fluctuations, u' into bins of uniform intervals to obtain a histogram of the data signal. The area of each histogram bin is then divided by the total area of the histogram, giving the probability density function of the time series.

Fig. 12a depicts the locations where velocity time signals are recorded for the LSB case with L and R being the label for those points in the vicinity of the left or right abutment, respectively. The probability density function (PDF) of the turbulent fluctuation of the streamwise velocity u', normalised by its root-mean-square value u'_{RMS} is calculated at each sampling point and plotted together with the Gaussian distribution (solid line). Fig. 12b plots the pdfs for the LSB's left abutment and as can be seen almost all the pdfs exhibit a skewness towards the positive except for the pdf at L1 which follows the Gaussian distribution fairly well. L1 is located in the vicinity of the tip of the abutment, where the separation begins. From L2 onwards, the pdfs show a clear deviation of the mean u'/u'_{RMS} from Gaussian towards the positive side, centred around $u'/u'_{RMS} = 0.4$ approx. The amplitude of the u' fluctuations is also skewed, ranging from $u'/u'_{RMS} = -4$ on the negative side of the axis to less than $u'/u'_{RMS} = 3$ on the positive values. This suggests that the flow at these locations feature many acceleration slightly stronger (than the average) accelerations due to the

bridge contraction (hence the positive u'/u'_{RMS} mean from L2 onwards) combined with more significant low frequency events in which the recirculation bubble expands into the shear layer along which points L2-L8 are located (hence the long negative tail of the PDFs). The seven R points located in the shear layer of the right abutment (Fig. 12c) follow quite closely the normal distribution, although with a very slight bias towards the negative side and a very slight tailing towards the positive side. This indicates a lower occurrence of high-momentum ejections from the right abutment's tip and a more balanced equilibrium between the recirculation and the main channel flow overall. The different turbulence characteristics in terms of streamwise velocity fluctuation of the flow around the two abutments is the consequence of the different abutment length (however not very significant in the LSB case) and the geometrical asymmetry of the compound channel; the left floodplain is much wider and carries more mass and momentum so that flow acceleration due to contraction is more significant in the shear layer of the left abutment than in the one of the right abutment.

Fig. 13 shows the locations where velocity time signals are recorded and the corresponding u'/u'_{RMS} pdfs for the SSB case. Overall, the pdfs at those points follow but amplify the trends from the LSB case, as it is expected given the greater contraction ratio. From the u'/u'_{RMS} pdfs along the left shear layer (L locations), only L2 appears to be Gaussian distributed. All other L signals exhibit a clear skewness, following the normal distribution up to $u'/u'_{RMS} = -1$, having a maximum at approx. $u'/u'_{RMS} = 0.75$ and then falling abruptly. The exception is L3, which peaks at approximately $u'/u'_{RMS} = -0.6$. L3 is situated at the point where small vortical eddies start to form shortly after the flow separates from the abutment tip. The behaviour of the points L2 and L4-L9 correlates with the frequent occurrence of ejections of high momentum flow (local accelerations) from the opening and low frequency events occur due to the expansion of the recirculation zone similar the LSB case. The meandering of the instantaneous velocities in the SSB setup as observed in Fig. 8a is the direct result of the oscillating recirculation zone. The pdfs at the locations near the right abutment (Fig. 13c) mostly follow the Gaussian distribution, except for R4 and R5 which are rather biased towards negative values on the u'/u'_{RMS} axis. This suggests a stronger recirculation

behind the right abutment that pushes the shear layer towards the main channel when compared to the LSB results. This correlates well with the observations made from Fig. 9b.

The quadrant analysis of the streamwise u'/u'_{RMS} and spanwise v'/u'_{RMS} velocity fluctuations are plotted in Figs. 14 and 15 for the LSB or SSB cases, respectively. Unlike the conventional quadrant analysis (Lu and Willmarth 1973) that investigates the sweeping and ejecting motion of the flow near the bed, here the analysis focuses on the horizontal turbulence events of the streamwise and spanwise directions in the separated shear layers. For brevity, only four points from each abutment are chosen and to be displayed and the vertical fluctuations w'/w'_{RMS} were omitted given the strong two-dimensional nature of the recirculations and the shear layers on the shallow floodplains. The location of the points is indicated in Figs. 12a and 13a, assuming positive directions for u'/u'_{RMS} and v'/u'_{RMS} east (flow towards the outlet) and north (flow towards the left side), respectively.

Fig. 14 shows the quadrant analysis for the LSB case. Points L3, L5, and L7 confirm the findings from Fig. 12b, with most points concentrated in Q1 ($u'/u'_{RMS} > 0$, $v'/u'_{RMS} > 0$) corresponding to fast-flow ejections from the contracted flow through the bridge opening, and fewer but higher-magnitude points recorded in Q3 ($u'/u'_{RMS} < 0$, $v'/u'_{RMS} < 0$), indicating lower-frequency intrusions of the recirculating flow in the shear layer. L1 exhibits a more balanced, isotropic trend, characterised by an oval shape which is characteristic of streamwise fluctuations. Points R3, R5, and R7 reproduce a more balanced oval shape dominated by Q2 and Q4 events ($u'/u'_{RMS} < 0$-$v'/u'_{RMS} > 0$ and $u'/u'_{RMS} > 0$-$v'/u'_{RMS} < 0$ respectively), as the relative position of floodplain and main channel switches from left to right abutment. Point R1, by the flow around abutment's tip has a slight tendency for Q2 and Q4 events but it is more isotropic than the other locations.

Fig. 15 shows the quadrant analysis for the SSB case. The data sampled at the L locations (left abutment) show three different patterns. At location L1, by the abutment tip, the data points show significant linearity in the axis Q2-Q4 ($u'/u'_{RMS} < 0$-$v'/u'_{RMS} > 0$ and $u'/u'_{RMS} > 0$-$v'/u'_{RMS} < 0$, respectively), revealing an almost one-dimensional flow, resembling a jet, as the water from the left floodplain is forced to pass around the abutment. At location L3 at which eddys start to form,

a more balanced, isotropic behaviour of the flow is observed, with a slight majority of turbulent events in Q3 ($u'/u'_{RMS} < 0$, $v'/u'_{RMS} < 0$) and fewer and more dispersed points in Q1 ($u'/u'_{RMS} > 0$, $v'/u'_{RMS} > 0$), indicating a dominance of the recirculation bubble at this location, with periodic intrusions of high-speed flow from the contraction, in agreement with the observations from Fig. 13b. The data at locations L5 and L7 are similarly in their oval shape and clustered around the u'/u'_{RMS} axis. The higher flow contraction induces strong acceleration and hence significant one-dimensionality of the flow, albeit the shift between positive and negative values of u'/u'_{RMS} reflects the meandering of the shear layer in the left abutment's shear layer. The flow is significantly anisotropic with u' having a greater variance than v'. Near the right abutment, the flow at R1 appears similar the flow at L1 (switching the axis from Q2-Q4 to Q1-Q3 due to the opposite orientation of the abutment) but is not quite as one-dimensional than at L1. At R3 the data show a rather isotropic distribution of turbulent events, that turns into an oval shape in the axis Q2-Q4 for R5 and R7 as small eddies roll up and being less one-dimensional than their left side counterparts.

Figs. 16-18 and Fig. 20 offer further insights into the turbulence structure at two chosen locations (L7 and R5) near each abutment and for both cases. Each figure consists of four sub-plots, from top-left to bottom-right: (a) power spectra of both the streamwise u' and the spanwise v' turbulent fluctuations in the domain of frequency (logarithmic scale) obtained through Fast Fourier Transformation; (b) power spectra in a semilog plot to identify high-energy events; c) out-of-plane vorticity contours ω_z, with white contours representing strong anti-clockwise motion ($\omega_z < 0$) and black contours representing strong clockwise motion ($\omega_z > 0$) (contours extracted at 0.015 m below the water surface); d) top view of the water surface ($\phi = 0$) at the same instant as in (c) to illustrate the correlation between the out-of-plane vorticity and the free surface undulation. The free surface is colour-coded with water depth where dark blue depicts the depressions in the water surface.

The power spectra from all four points (Figs. 16a - 18a and 20a) follow the -5/3 slope, indicating homogenous turbulence, before a faster decay of energy is observed at higher frequencies which is mainly induced by the SGS model. The plots demonstrate that the inertial sub-range

of the energy cascade for u' and v' is well resolved that the fine mesh resolves satisfactorily the energy-containing scales of the flow. In total over two frequency decades of the flow, between the production of energetic large-scale vortices and the dissipation of the small scale turbulence are resolved by the LES of both cases.

Fig. 16 reveals the vortex shedding at L7, located downstream of the left abutment of the LSB setup. The power spectra of u' and v' at L7 show a very distinct peak at approximately 0.1 Hz, revealing the persistent occurrence of a turbulent event with a 10 s periodicity. This peak is particularly well depicted in Fig. 16b, where the logarithmic scale for the spectral amplitude of the velocity signal has been removed. This event captured in the spectral analysis is a vortex that rolls up in the shear layer downstream of the left abutment which is convected downstream. The area of high vorticity ω_z in Fig. 16c and the depressions in the water surface map Fig. 16d (indicated with arrows) visualise two of these vortices each at a different stage their evolution. The vortex closer to the abutment (above the left arrow) has just rolled up whereas the vortex further downstream (above right arrow) has reached its maximum size and is being convected by the flow downstream. The average period of occurence of this vortex is approximately 10 s. The vortex can also be identified from the quadrant analysis at L7 (Fig.14), where the dominant high-frequency $u' > 0$ ejections are complemented with few but significant (low-frequency) $u' < 0$ events the signature of the passing vortex.

Fig. 17 quantifies periodical turbulent events at R5, i.e. downstream of the right abutment of the LSB case. The u' spectrum (Figs. 17a-b) exhibits two high-energy peaks which correspond to approx. 10s and 6.2s periodicity (or in terms of frequency to 0.1 Hz and 0.16 Hz, respectively). The latter peak is also seen in the v' spectrum. The ω_z contours and water surface maps (Figs. 17c-d) reveal vortex roll-up and shedding from the tip of the abutment, albeit more irregular than around the left abutment. The vortex generation and roll-up are highlighted with arrows in Figs. 17c-d. Unlike the left abutment, there appears to be a bi-modality in the vortex formation, also just noticable in the equivalent pdf (12c). This bi-modal behavior is probably due the interaction of the vortex with the secondary flow near the main channel-floodplain interface, dominated by the SSL,

IV and NV vortices described in Fig. 10.

Fig. 18 reveals large-scale turbulence at L7, downstream of the left abutment of the SSB case. The u' energy spectra (Figs. 18a-b) exhibit a very prominent low-frequency peak at 0.1 Hz (10 s period). However, the vortices (Figs. 18c) do not appear to roll-up into distinct eddies such as those seen behind the LSB abutment, but rather are stretched due to the strong acceleration and stay within a narrow band along the shear layer. The water surface elevation plot (Fig. 18d) does not depict significant depressions suggesting the absence of a well-defined eddy downstream of the left abutment and this can also be concluded from the fact that the v' spectra do not show any low-frequency peak. Moreover, the quadrant analysis (Fig. 15) also reveals the jet-like acceleration (almost one-dimensional flow) due to the narrow bridge opening with significantly greater u' than v' values. From animations of the flow downstream of the abutment it is seen that the 10s-periodicity correlates with a low-frequency meandering of the main channel flow as visualised by the instantaneous streamwise velocity flow field depicted in Fig. 8a.

Fig. 19 (top) shows a time series of the instantaneous streamwise velocity at L7 where distinctive high- and low-velocity peaks occur approximately every 10 s. The instantaneous streamwise velocity u contours at the six instants in time labelled in the time series (t_1-t_6) are also presented below the timeseries to illustrate the shift between high velocities (dominant most of the time) and sudden low velocity peaks (at t_2, t_4 and t_6). Two black lines representing 0.2 m/s and 0.4 m/s contours are included in the figure to highlight the boundary between the recirculation bubble and the main flow. This boundary oscillates due to the combination of the vorticity generated by the ejections from the bridge opening and the secondary flow at the main channel-floodplain interface, resulting in the characteristic 0.1 Hz meandering motion.

The turbulence characteristic at R5, downstream of the right abutment of the SSB case, is revealed with Fig. 20. The power spectra (Figs. 20a-b) show multiple peaks ranging from 0.1 Hz to 0.47 Hz, that can be correlated with several eddies (with periods between 2-10 s approx.) springing off the right abutment's tip as can be appreciated from Figs. 20c-d. The flow in this location is similar to the one behind the LSB abutment, however the relatively small peaks in the

v' spectra indicate that the flow accelerates at the right abutment in a similar fashion to the left abutment, which leads to more irregular shedding of vortices. The irregularity of vortex shedding is, similarly to the LSB case, due to the interplay of SSL, IV and NV vortices.

CONCLUSION

In this study the method of large eddy simulation (LES) has been employed to elucidate and quantify the flow and associated turbulence structures around bridge abutments of different lengths, i.e. a long setback (LSB) abutment and a short setback (SSB) abutment, which are placed in a compound and asymmetric channel. A free surface algorithm has been included in the LES which has allowed predicting the free-surface deformation of the two investigated scenarios. Experimental data has been used to validate the two simulations and very convincing agreement of computed streamwise velocity profiles with the measured ones has been found. Similarly good agreement of LES-computed water surface elevations with experimental data has been observed and has thus established the credibility of the numerical method. The simulations have allowed the quantification of the effect of the abutment length on the flow and turbulence through and behind the bridge opening. Moreover, instantaneous and time-averaged streamwise velocity contours have been plotted and analysed to reveal several key differences between the SSB and LSB flow scenarios: a) a significantly larger recirculation zone downstream of the left abutment but a smaller corner vortex in in SSB scenario in comparison with the LSB scenario; b) the main channel flow in the SSB scenario is skewed more clearly towards the right bank due to the more accelerated flow and the larger recirculation zone downstream of the abutment of the SSB scenario; and c) more significant meandering of the flow downstream of the abutment in the SSB scenario. In addition, turbulence structures, such as rolled-up shear layer-, necklace- and interface vortices due to the secondary flow, generated by the abutments and/or the compound channel geometry, respectively, have been visualised using isosurfaces of the Q-criterion and out-of-plane vorticity contours. The differences between the LSB and SSB flow scenarios are: a) only in the SSB scenario, a very well-defined longitudinal (or streamwise) vortex is found at the interface between the main channel and the left floodplain; b) only in the LSB scenario, a pair of counter-rotating vortices appears near the surface

in the vicinity of the left floodplain, being reflected in the free surface deformation in the form of a persistent bulging line. Further analysis of the prevailing turbulence structures has been carried out using three different techniques: probability density functions, quadrant analysis and power density spectra. The analyses of the time series of instantaneous velocity signals has quantified the complex turbulent flow near the abutments including: a) frequent occurrence of ejections of high momentum flow in the form of vortices springing-off of the tip of the abutment and rolling-up into low-frequency horizontal vortices in the vicinity of the long setback abutment and b) domination of strongly-accelerated flow in the vicinity of the short setback abutment due to the higher contraction. This jet-like flow is pretty-much one-dimensional and persists over a substantial distance downstream. c) wake-meandering flow downstream of the short-setback abutment and d) irregular vortex generation and shedding at the right abutment (in both cases) due to the interaction of main-channel/floodplain interface vortices.

ACKNOWLEDGEMENT

This work was sponsored by the American Association of State Highway and Transportation Officials (AASHTO), in cooperation with the Federal Highway Administration, and was conducted in the National Cooperative Highway Research Program (NCHRP), which is administered by the Transportation Research Board (TRB) of the National Academics of Sciences, Engineering, and Medicine. The authors acknowledge the support of the Supercomputing Wales project, which is part-funded by the European Regional Development Fund (ERDF) via Welsh Government

NOTATION

The following symbols are used in this paper:

Fr = Froude number;

ϕ = level set signed distance function;

Ω_{gas} = Fluid domain for gas;

Ω_{liquid} = Fluid domain for water;

Γ = Water surface interface;

B_f = Left floodplain width;

U_b = Bulk streamwise velocity;

Re = Reynolds number;

h = Initial free surface height;

b = Width of channel;

x/b = Streamwise distance normalised by width of channel;

u = Instantaneous streamwise velocity;

$< u >$ = Time-averaged streamwise velocity;

X_{LSB} = Time-averaged length of recirculation bubbles in LSB;

X_{SSB} = Time-averaged length of recirculation bubbles in SSB;

U_{LSB} = Maximum streamwise velocity in LSB;

U_{SSB} = Maximum streamwise velocity in SSB;

Q = Q-criterion;

$|\Omega|$ = Rotation rate;

$|S|$ = Strain rate;

u_i, u_j = Instantaneous velocity components;

ω_x = Streamwise vorticity;

u' = Turbulent fluctuation of streamwise velocity;

u'_{RMS} = Root-mean-square of turbulent fluctuation of streamwise velocity; and

v' = Turbulent fluctuation of spanwise velocity.

REFERENCES

Bomminayuni, S. K. and Stoesser, T. (2011). "Turbulence Statistics in an Open-Channel Flow over a Rough Bed." *Journal of Hydraulic Engineering*, 137(11), 1347–1358.

Cater, J. E. and Williams, J. J. R. (2008). "Large eddy simulation of a long asymmetric compound open channel." *Journal of Hydraulic Research*, 46(4), 445–453.

Dubief, Y. and Delcayre, F. (2000). "On coherent-vortex identification in turbulence." *Journal of Turbulence*, 1(January), 1–22.

Ettema, R., Nakato, T., and Muste, M. (2010). "Estimation of Scour Depth At Bridge Abutments." *Report No. January*, The University of Iowa, Iowa.

Fael, C. M. S., Simarro-Grande, G., Martín-Vide, J. P., and Cardoso, A. H. (2006). "Local scour at vertical-wall abutments under clear-water flow conditions." *Water Resources Research*, 42(10), 1–12.

Fraga, B. and Stoesser, T. (2016). "Influence of bubble size, diffuser width, and flow rate on the integral behavior of bubble plumes." 121, 3887–3904.

Fraga, B., Stoesser, T., Lai, C. C. K., and Socolofsky, S. A. (2016). "A LES-based Eulerian-Lagrangian approach to predict the dynamics of bubble plumes." *Ocean Modelling*, 97, 27–36.

Hong, S. H. (2012). "Prediction of Clear-Water Abutment Scour Depth in Compound Channel for Extreme Hydrologic Events." Ph.D. thesis, Georgia Institute of Technology, <https://smartech.gatech.edu/handle/1853/47535> (dec).

Hong, S. H., Sturm, T. W., and Stoesser, T. (2015). "Clear Water Abutment Scour in a Compound Channel for Extreme Hydrologic Events." *Journal of Hydraulic Engineering*, 141(6).

Kang, S. and Sotiropoulos, F. (2012). "Numerical modeling of 3D turbulent free surface flow in natural waterways." *Advances in Water Resources*, 40, 23–36.

Kara, S., Kara, M. C., Stoesser, T., and Sturm, T. W. (2015). "Free-Surface versus Rigid-Lid LES Computations for Bridge-Abutment Flow." *Journal of Hydraulic Engineering*, 141(9).

Kara, S., Stoesser, T., and Sturm, T. W. (2012). "Turbulence statistics in compound channels with deep and shallow overbank flows." *Journal of Hydraulic Research*, 50(5), 482–493.

584 Koken, M. (2011). "Coherent structures around isolated spur dikes at various approach flow an-
585 gles." *Journal of Hydraulic Research*, 49(6), 736–743.
586 Koken, M. (2017). "Coherent structures at different contraction ratios caused by two spill-through
587 abutments." *Journal of Hydraulic Research*, homepage, 22–1686.
588 Koken, M. and Constantinescu, G. (2008a). "An investigation of the flow and scour mechanisms
589 around isolated spur dikes in a shallow open channel: 1. Conditions corresponding to the initia-
590 tion of the erosion and deposition process." *Water Resources Research*, 44(8), 1–19.
591 Koken, M. and Constantinescu, G. (2008b). "An investigation of the flow and scour mechanisms
592 around isolated spur dikes in a shallow open channel: 2. Conditions corresponding to the final
593 stages of the erosion and deposition process." *Water Resources Research*, 44(8).
594 Koken, M. and Constantinescu, G. (2009). "An investigation of the dynamics of coherent structures
595 in a turbulent channel flow with a vertical sidewall obstruction." *Physics of Fluids*, 21(8).
596 Koken, M. and Constantinescu, G. (2014). "Flow and Turbulence Structure around Abutments with
597 Sloped Sidewalls." *Journal of Hydraulic Engineering*, 140(7), 04014031.
598 Laursen, E. M. (1963). "An analysis of relief bridge scour." *Journal of the Hydraulics Division*.
599 Lin, C., Han, J., Bennett, C., and Parsons, R. L. (2014). "Case History Analysis of Bridge Failures
600 due to Scour." *Climatic Effects on Pavement . . .* , 1–13.
601 Liu, Y., Stoesser, T., Fang, H., Papanicolaou, A., and Tsakiris, A. G. (2016). "Turbulent flow over
602 an array of boulders placed on a rough, permeable bed." *Computers and Fluids*, 158, 120–132.
603 Lu, S. S. and Willmarth, W. W. (1973). "Measurements of the structure of the Reynolds stress in a
604 turbulent boundary layer." *Journal of Fluid Mechanics*, 60(03), 481.
605 McSherry, R., Chua, K., Stoesser, T., and Mulahasan, S. (2018). "Free surface flow over square
606 bars at intermediate relative submergence." *Journal of Hydraulic Research*, 1–19.
607 Melville, B. W. (1992). "Local scour at bridge piers." *Journal of Hydraulic Engineering*, 118(4),
608 615–631.
609 Melville, B. W. (1995). "Bridge Abutment Scour in Compound Channels." *Journal of Hydraulic*
610 *Engineering*, 121(12), 863–868.

611 Nicoud, F. and Ducros, F. (1999). "Subgrid-scale stress modelling based on the square of the
612 velocity gradient tensor." *Flow, turbulence and Combustion*, 62(3), 183–200.
613 Osher, S. and Sethian, J. A. (1988). "Fronts propagating with curvature-dependent speed: Al-
614 gorithms based on Hamilton-Jacobi formulations." *Journal of Computational Physics*, 79(1),
615 12–49.
616 Ouro, P., Harrold, M., Stoesser, T., and Bromley, P. (2017a). "Hydrodynamic loadings on a hori-
617 zontal axis tidal turbine prototype." *Journal of Fluids and Structures*, 71, 78–95.
618 Ouro, P. and Stoesser, T. (2017). "An immersed boundary-based large-eddy simulation approach
619 to predict the performance of vertical axis tidal turbines." *Computers & Fluids*, 152, 74–87.
620 Ouro, P., Wilson, C. A., Evans, P., and Angeloudis, A. (2017b). "Large-eddy simulation of shallow
621 turbulent wakes behind a conical island." *Physics of Fluids*, 29(12).
622 Paik, J. and Sotiropoulos, F. (2005). "Coherent structure dynamics upstream of a long rectangular
623 block at the side of a large aspect ratio channel." *Physics of Fluids*, 17(11), 1–14.
624 Rodi, W., Constantinescu, G., and Stoesser, T. (2013). *Large-eddy simulation in hydraulics*. Crc
625 Press.
626 Shirole, A. and Holt, R. (1991). "Planning for a comprehensive bridge safety assurance program."
627 *Transport Research Record*, Vol. 1290, 137–142.
628 Stoesser, T. (2010). "Physically Realistic Roughness Closure Scheme to Simulate Turbulent Chan-
629 nel Flow over Rough Beds within the Framework of LES." *Journal of Hydraulic Engineering*,
630 136(10), 812–819.
631 Stoesser, T. (2014). "Large-eddy simulation in hydraulics: Quo Vadis?." *Journal of Hydraulic*
632 *Research*, 52(4), 441–452.
633 Stoesser, T., McSherry, R., and Fraga, B. (2015). "Secondary Currents and Turbulence over a
634 Non-Uniformly Roughened Open-Channel Bed." *Water*, 7(9), 4896–4913.
635 Stoesser, T. and Nikora, V. (2008). "Flow structure over square bars at intermediate submergence:
636 Large Eddy Simulation study of bar spacing effect." *Acta Geophysica*, 56(3), 876–893.
637 Sturm, T. W. (2006). "Scour around Bankline and Setback Abutments in Compound Channels."

638 *Journal of Hydraulic Engineering*, 132(1), 21–32.

639 Sturm, T. W. and Janjua, N. S. (1994). "Clear-water Scour Around Abutments in Floodplains."
640 *Journal of Hydraulic Engineering*, 120(8), 956–972.

641 Sumer, B. M. and Fredsøe, J. (2002). *The Mechanics of Scour in the Marine Envi-*
642 *ronment*, Vol. 17 of *Advanced Series on Ocean Engineering*. WORLD SCIENTIFIC,
643 <http://www.worldscientific.com/worldscibooks/10.1142/4942> (apr).

644 Sussman, M., Smereka, P., and Osher, S. (1994). "A Level Set Ap-
645 proach for Computing Solutions to Incompressible Two-Phase Flow,
646 <http://www.sciencedirect.com/science/article/pii/S0021999184711557>.

647 Wardhana, K. and Hadipriono, F. C. (2003). "Analysis of Recent Bridge Failures in the United
648 States." *Journal of Performance of Constructed Facilities*, 17(3), 144–150.

649 Xie, Z., Lin, B., and Falconer, R. A. (2013). "Large-eddy simulation of the turbulent structure in
650 compound open-channel flows." *Advances in Water Resources*, 53, 66–75.

651 Yue, W., Lin, C.-L., and Patel, V. C. (2005). "Large eddy simulation of turbulent open-channel
652 flow with free surface simulated by level set method." *Physics of Fluids*, 17(2), 025108.

653 Yue, W., Lin, C.-L., and Patel, V. C. (2006). "Large-Eddy Simulation of Turbulent Flow over a
654 Fixed Two-Dimensional Dune." *Journal of Hydraulic Engineering*, 132(7), 643–651.

List of Figures

Fig. 1. Computational domains: (a) Long-setback abutment case, LSB, (b) Short-setback abutment case, SSB, (c) Cross-section including its dimensions.

Fig. 2. Definition sketch of the abutments and bridge area. The intersections between horizontal numbered lines (1-5) and vertical solid (LSB) and dashed (SSB) lines indicate the locations at which time-averaged streamwise velocity profiles (a)-(h) were measured experimentally.

Fig. 3. Computed and measured time-averaged streamwise velocity profiles at locations (a)-(h) (as described in Fig. 2) in cross-sections 2-4 of the LSB case. Experimental data (circles), coarse-mesh LES (dashed line), and fine-mesh LES (solid line).

Fig. 4. Computed and measured time-averaged streamwise velocity profiles at locations [a]-[h] (as described in Fig. 2) in cross-sections 2-4 of the SSB case. Experimental data (circles), coarse-mesh LES (dashed line), and fine-mesh LES (solid line).

Fig. 5. Computed (solid line) and measured (circles) profiles of the water surface for the LSB case at cross-section 2-4.

Fig. 6. Computed (solid line) and measured (circles) profiles of the water surface for the SSB case at cross-section 2-4.

Fig. 7. LES-predicted streamwise velocity contours in a selected horizontal plane: (a) instantaneous (b) time-averaged velocity for the LSB case.

Fig. 8. LES-predicted streamwise velocity contours in a selected horizontal plane: (a) instantaneous (b) time-averaged velocity for the SSB case.

Fig. 9. 2D streamlines near the abutment for (a) the LSB case and (b) the SSB case, 3D streamlines colour-coded with time-averaged streamwise velocity for (a) the LSB case and (b) the SSB case.

Fig. 10. Isosurfaces of the Q-criterion together with contours of the streamwise vorticity in selected cross-sections: (a) LSB case, (b) SSB case.

Fig. 11. Water surface deformation represented by zero level set and colour-coded by water depth for (a)LSB case and (b) SSB case.

Fig. 12. LSB case: (a) Locations along the estimated separated shear layer where velocity time signals are recorded. (b) Probability density function of streamwise velocity fluctuation normalised by the root-mean-square of the streamwise velocity fluctuation near the left abutment at all locations and (c) Probability density function of streamwise velocity fluctuation at all locations in the vicinity of the right abutment.

Fig. 13. SSB case: (a) Locations along the estimated separated shear layer where velocity time signals are recorded. (b) Probability density function of streamwise velocity fluctuation normalised by the root-mean-square of the streamwise velocity fluctuation near the left abutment at all locations and (c) Probability density function of streamwise velocity fluctuation at all location in the vicinity of the right abutment.

Fig. 14. Quadrant analysis of the streamwise and spanwise velocity fluctuation normalised with u'_{RMS} for the LSB case.

Fig. 15. Quadrant analysis of the streamwise and spanwise velocity fluctuation normalised with u'_{RMS} for the SSB case.

Fig. 16. Power spectra of a streamwise and spanwise velocity fluctuation time series at location L7: (a) in log-log scale, (b) in semi-log scale, (c) out-of-plane vorticity contours in a horizontal plane near the water surface and (d) water surface represented by zero level set colour-coded by the water depth for the LSB case.

Fig. 17. Power spectra of a streamwise and spanwise velocity fluctuation time series at location R5: (a) in log-log scale, (b) in semi-log scale, (c) out-of-plane vorticity contours in a horizontal plane near the water surface and (d) water surface represented by zero level set colour-coded by the water depth for the LSB case.

Fig. 18. Power spectra of a streamwise and spanwise velocity fluctuation time series at location L7: (a) in log-log scale, (b) in semi-log scale, (c) out-of-plane vorticity contours in a horizontal plane near the water surface and (d) water surface represented by zero level set colour-coded by the water depth for the SSB case.

Fig. 19. Time series of the streamwise velocity at location L7 of the SSB case and streamwise velocity contours at six selected instants in time labeled t_1-t_6.

Fig. 20. Power spectra of a streamwise and spanwise velocity fluctuation time series at location R5: (a) in log-log scale, (b) in semi-log scale, (c) out-of-plane vorticity contours in a horizontal plane near the water surface and (d) water surface represented by zero level set colour-coded by the water depth for the SSB case.

Figure 1

Click here to access/download;Figure;fig1.tiff

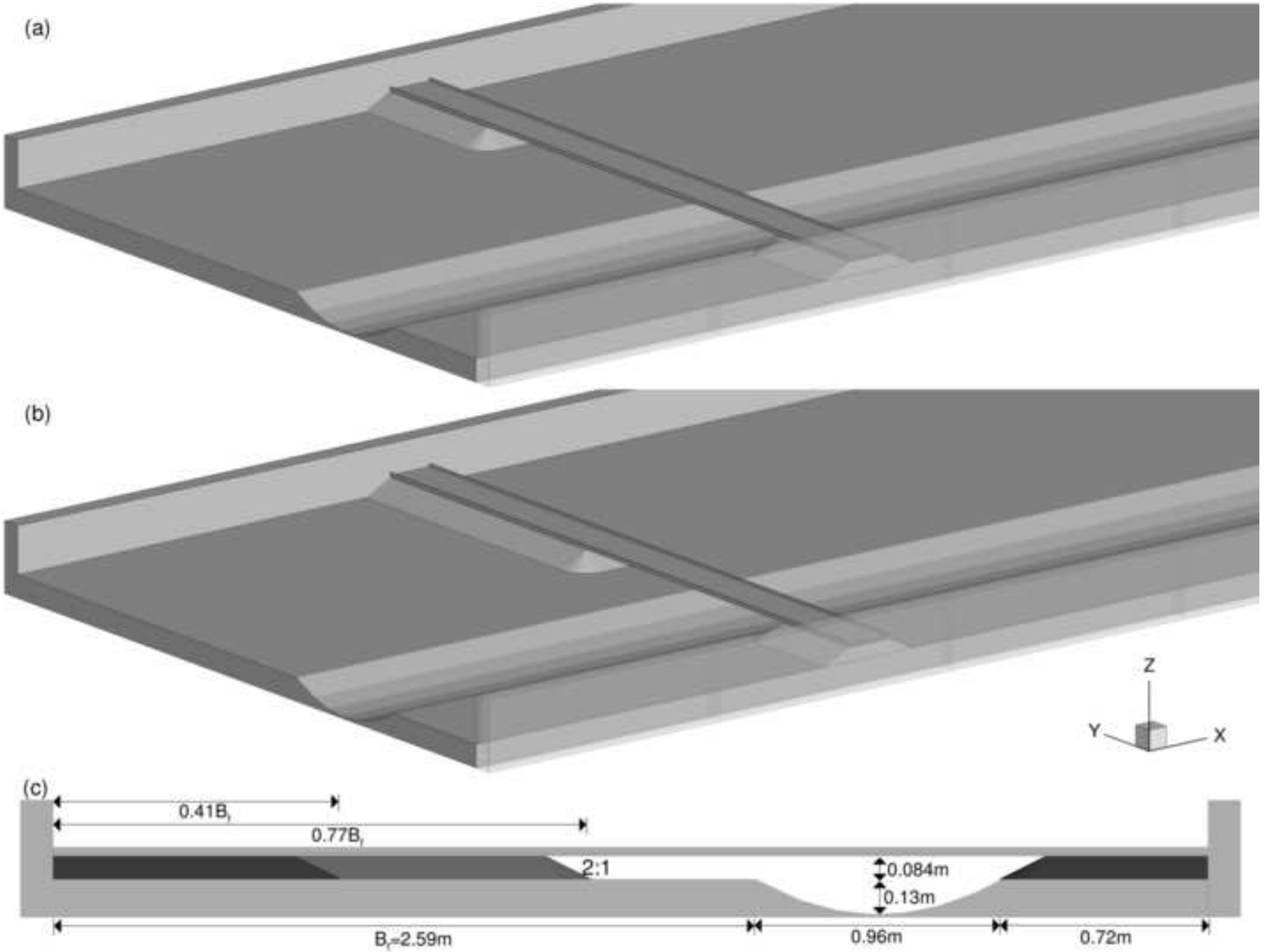

Figure 2

Click here to access/download;Figure;fig2.tiff

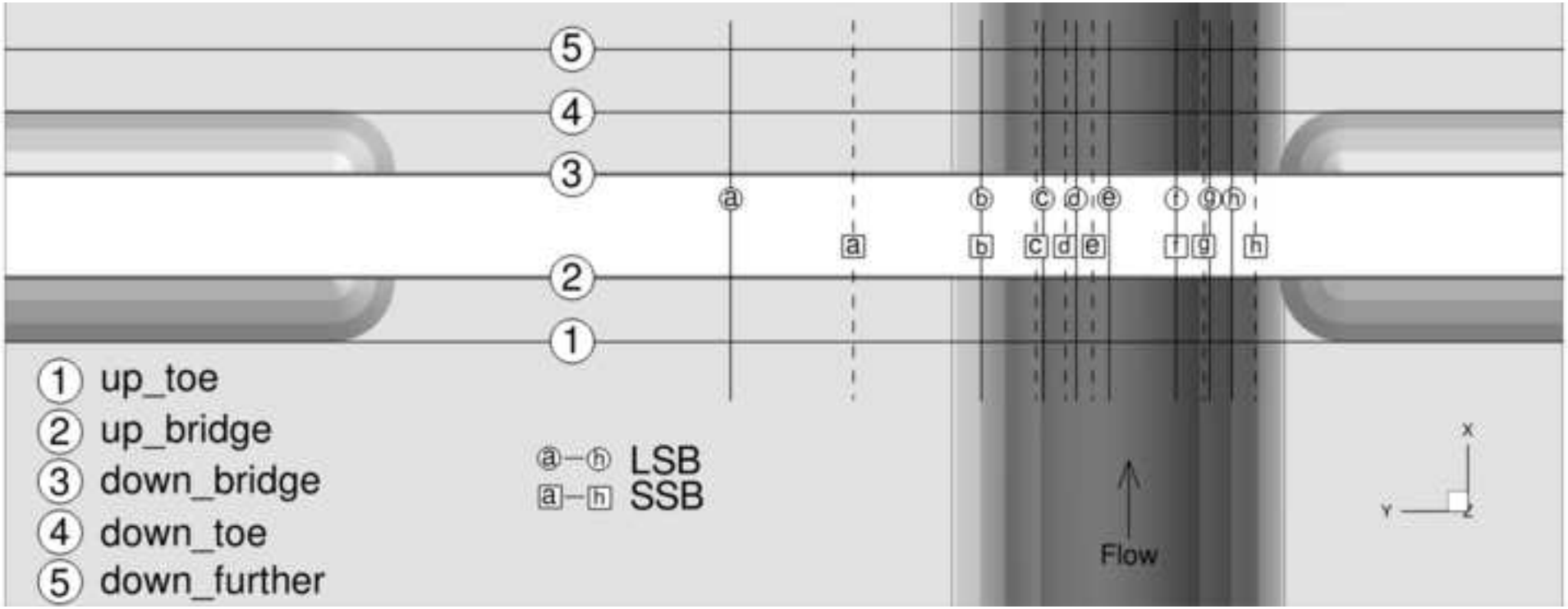

Figure 3

Click here to access/download;Figure;fig3.tiff

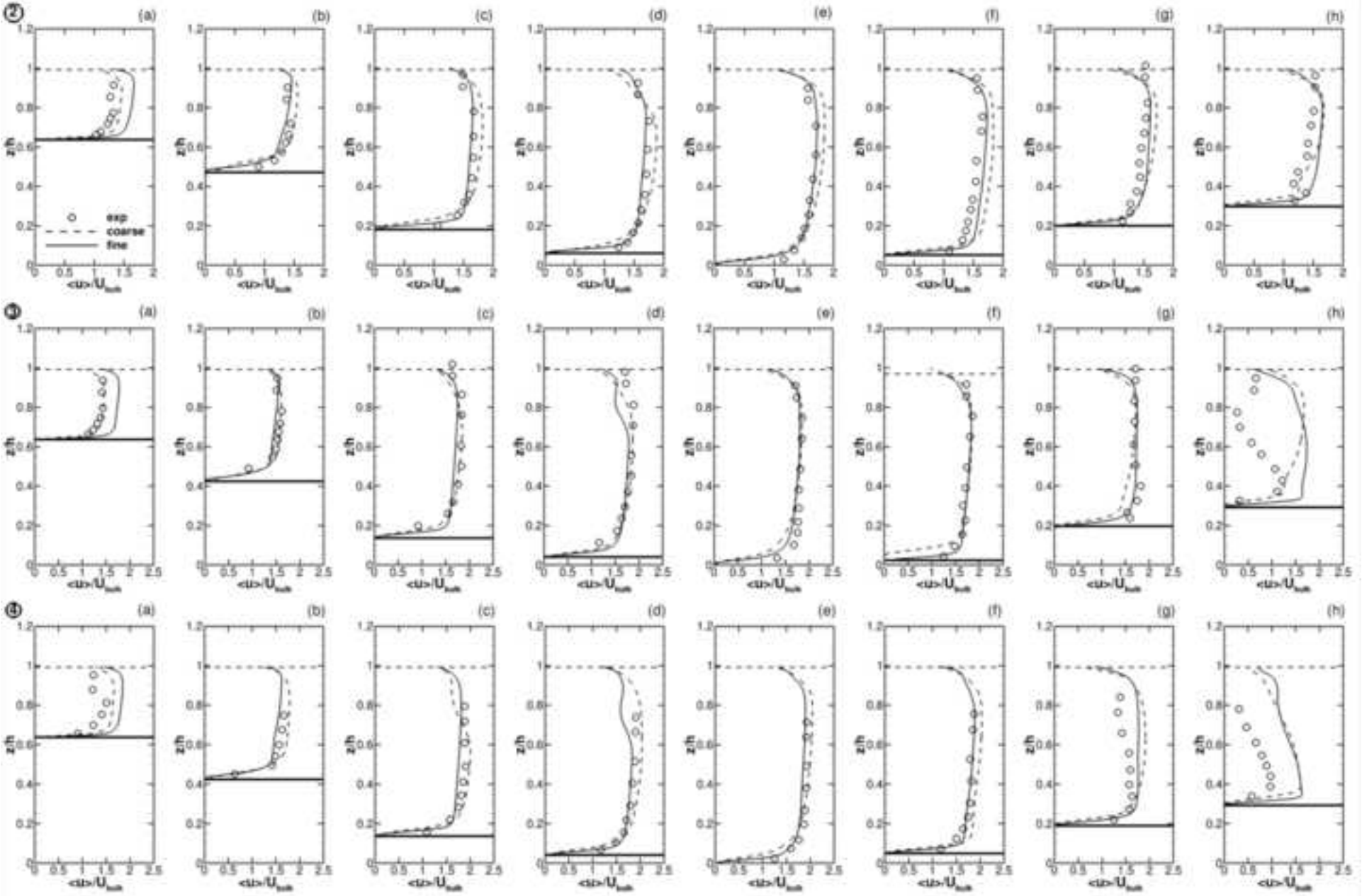

Figure 4

Click here to access/download;Figure;fig4.tiff

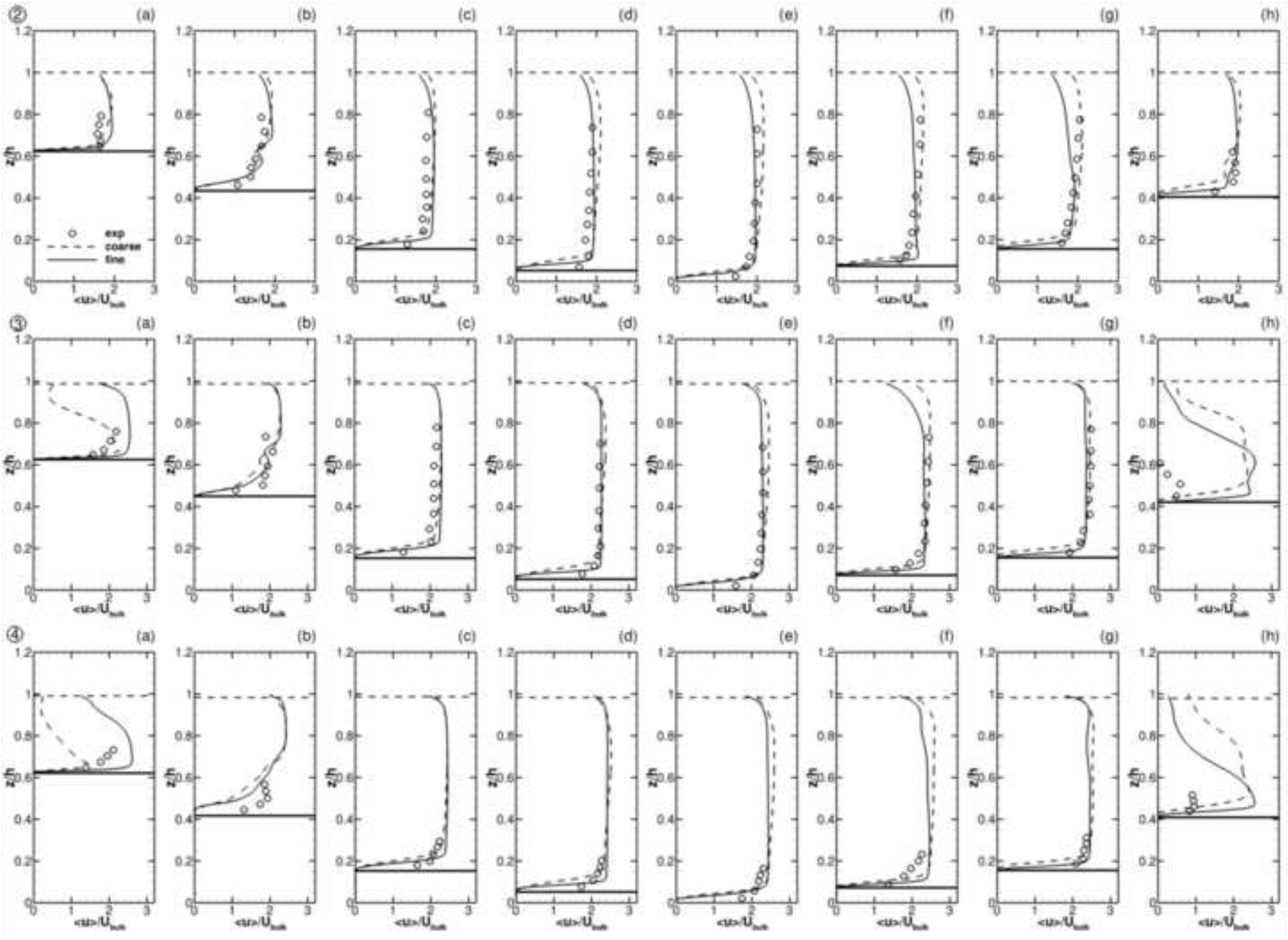

Figure 5

Click here to access/download;Figure;fig5.tiff

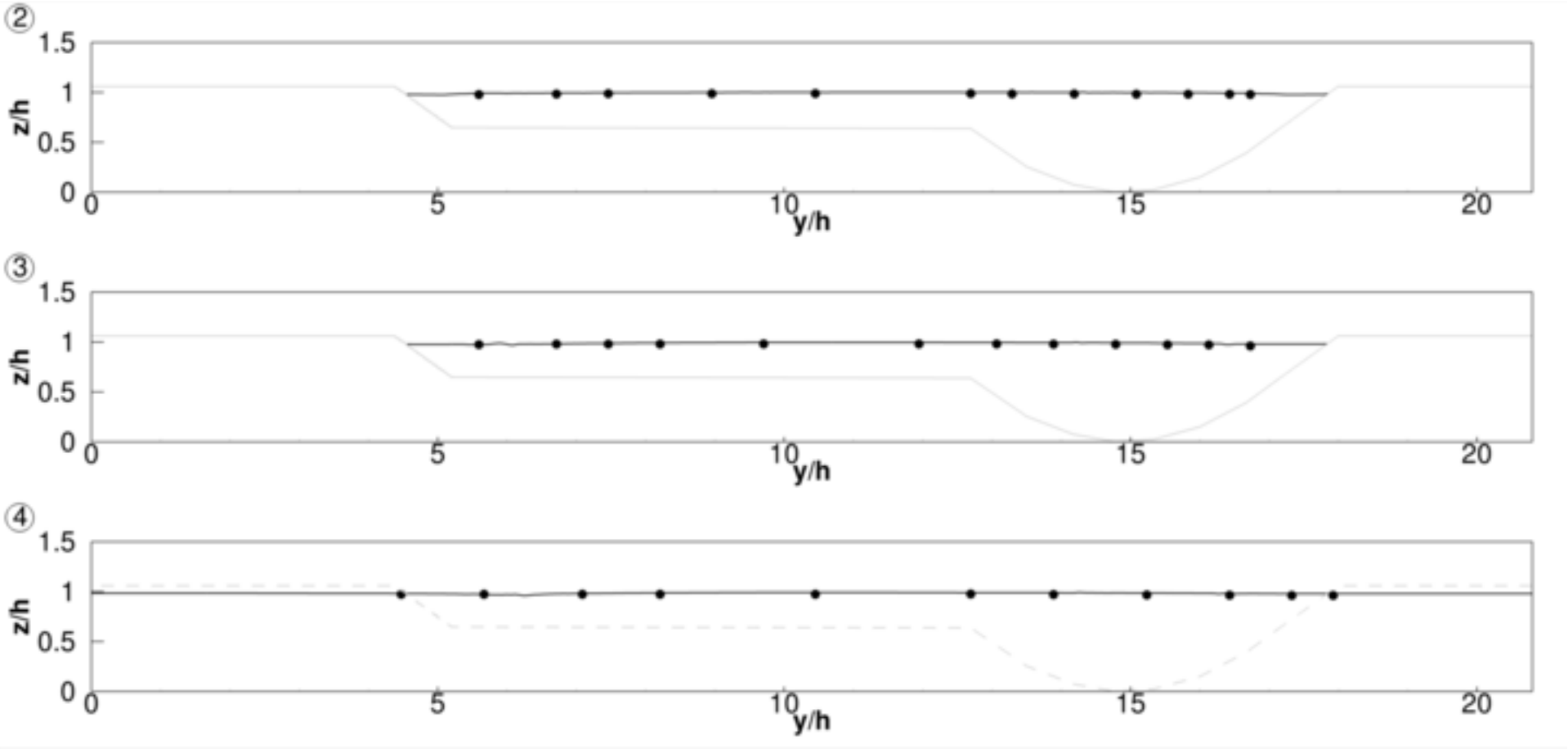

Figure 6

Click here to access/download;Figure;fig6.tiff

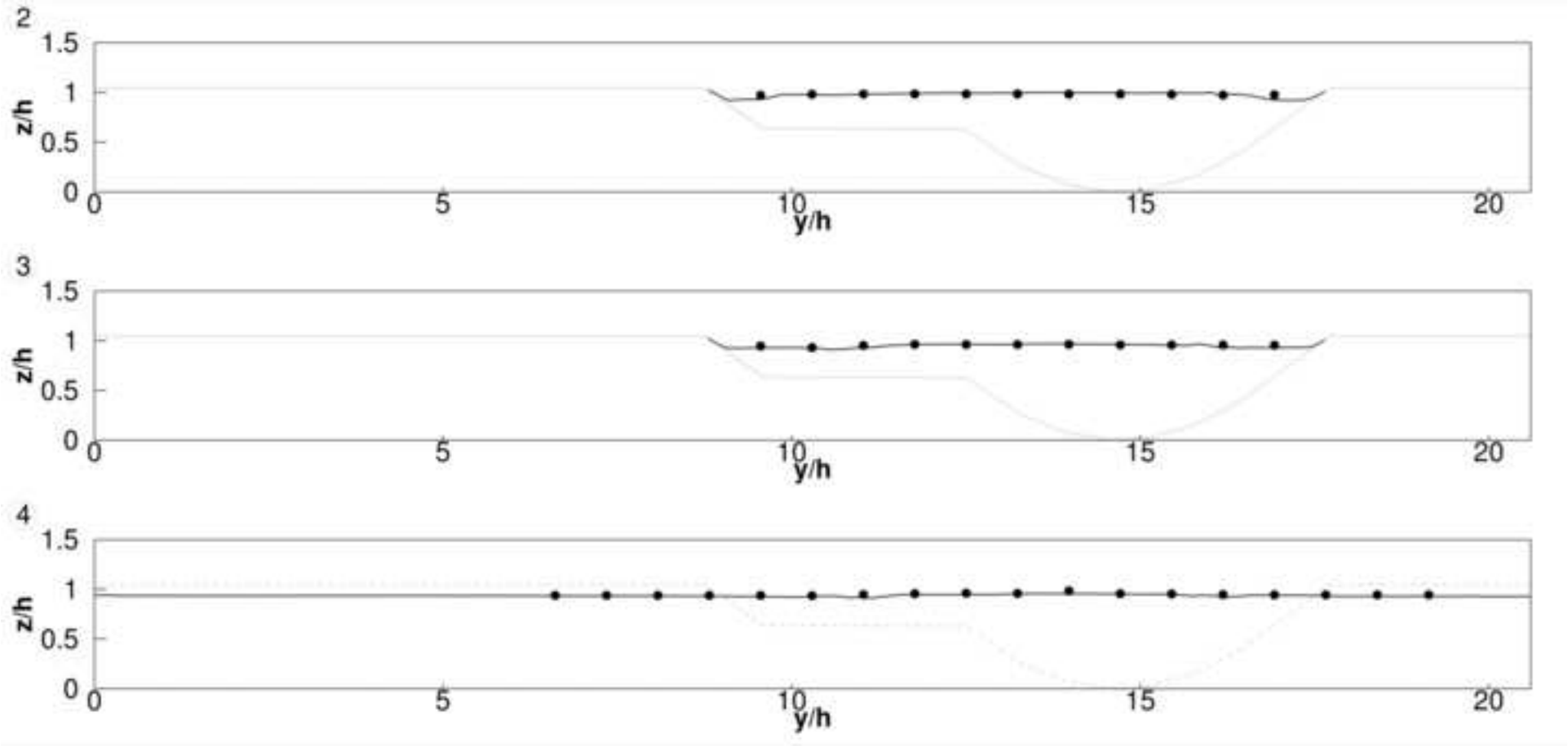

Figure 7

Click here to access/download;Figure;fig7.tiff

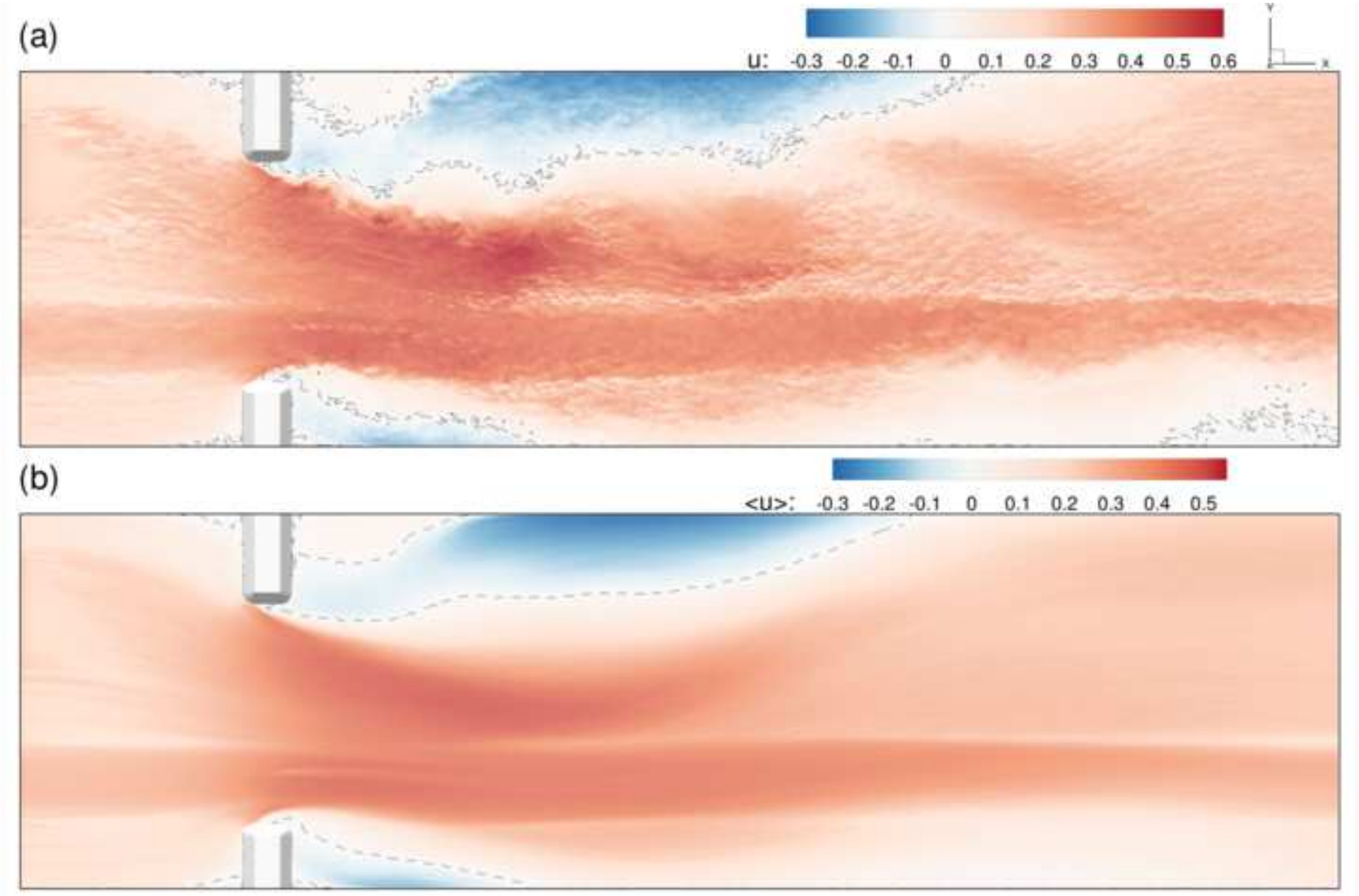

Figure 8

Click here to access/download;Figure;fig8.tiff

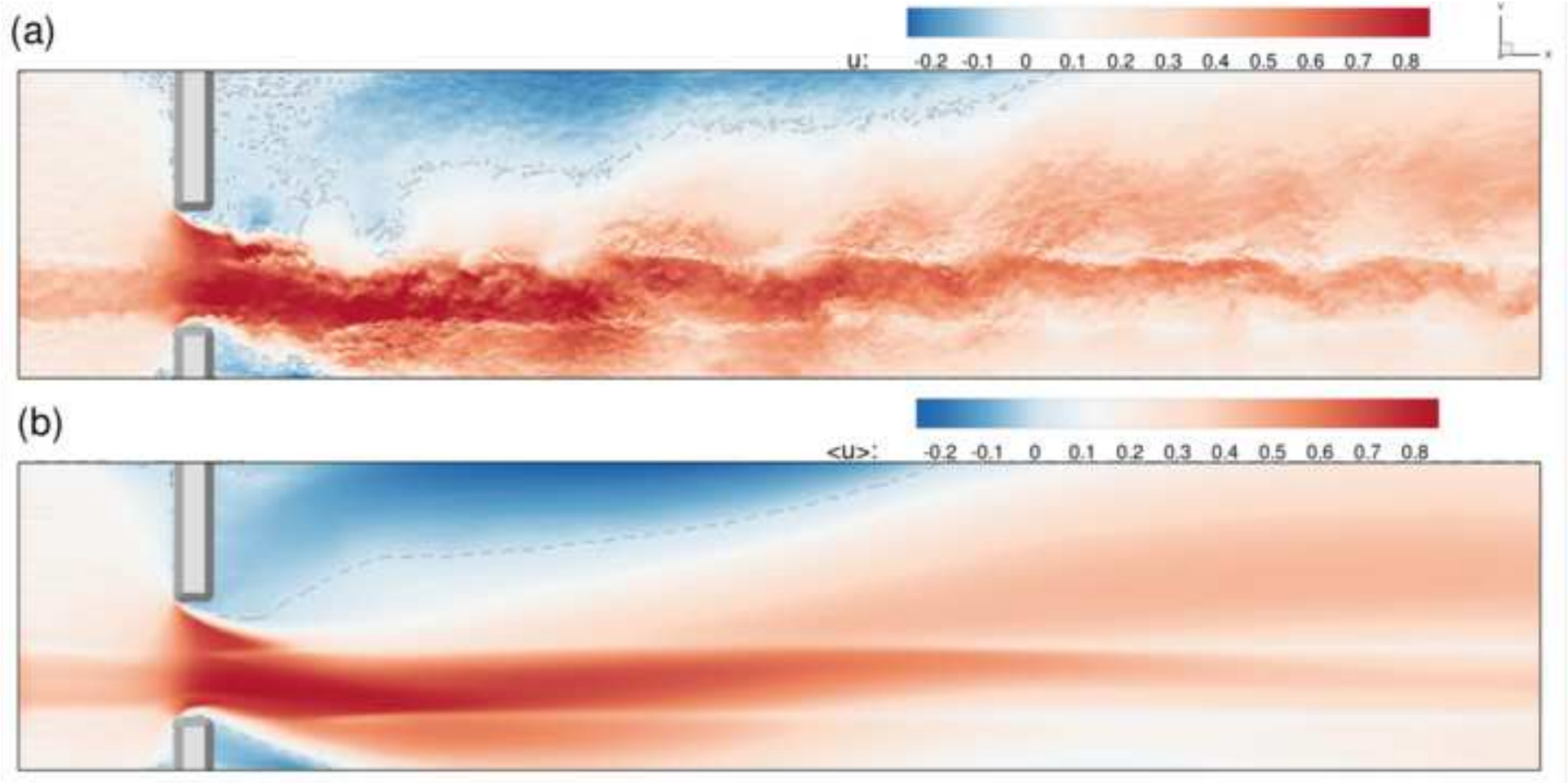

Figure 9

Click here to access/download;Figure;fig9.tiff

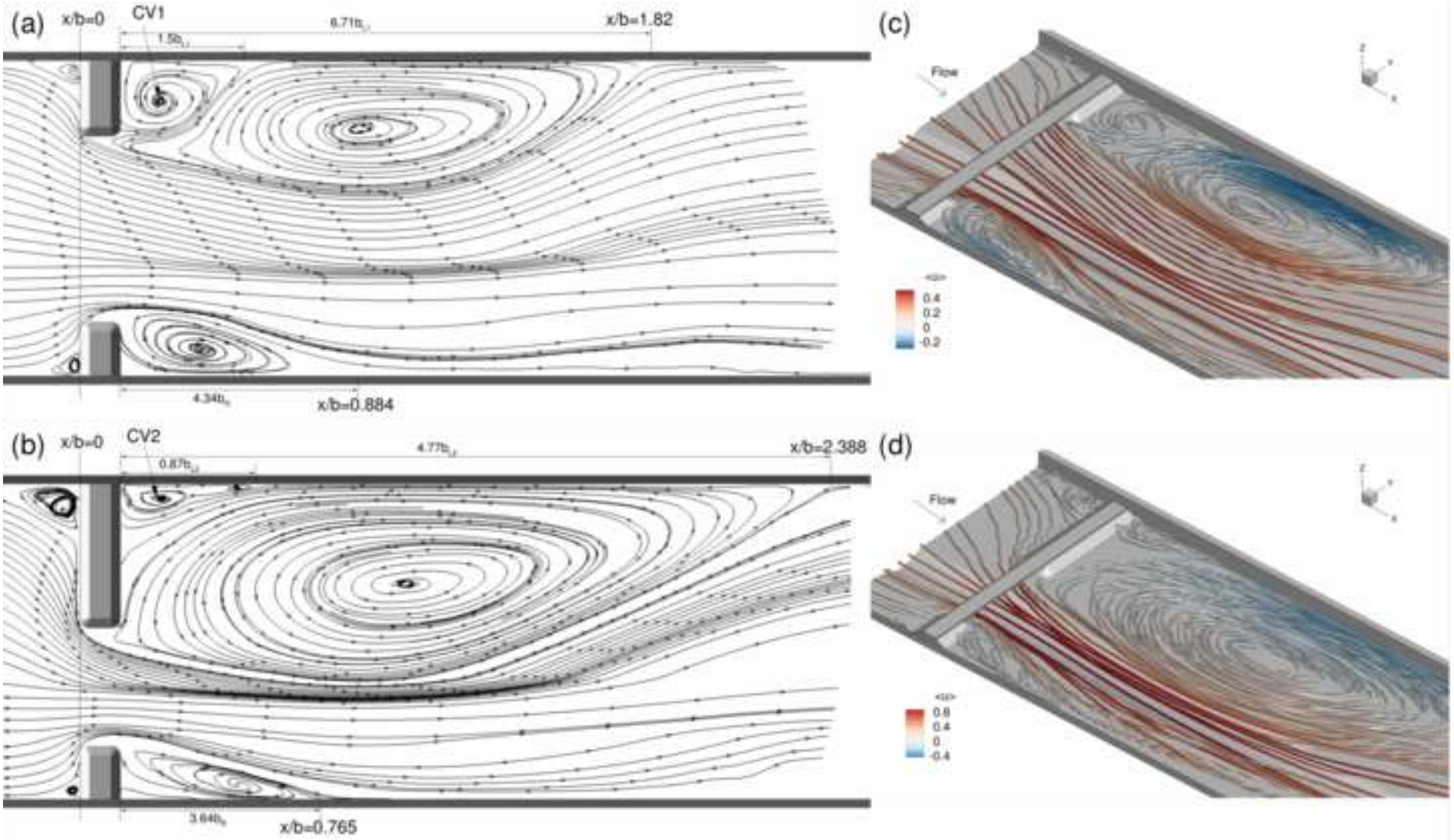

Figure 10a

Click here to access/download;Figure;fig10a.tiff

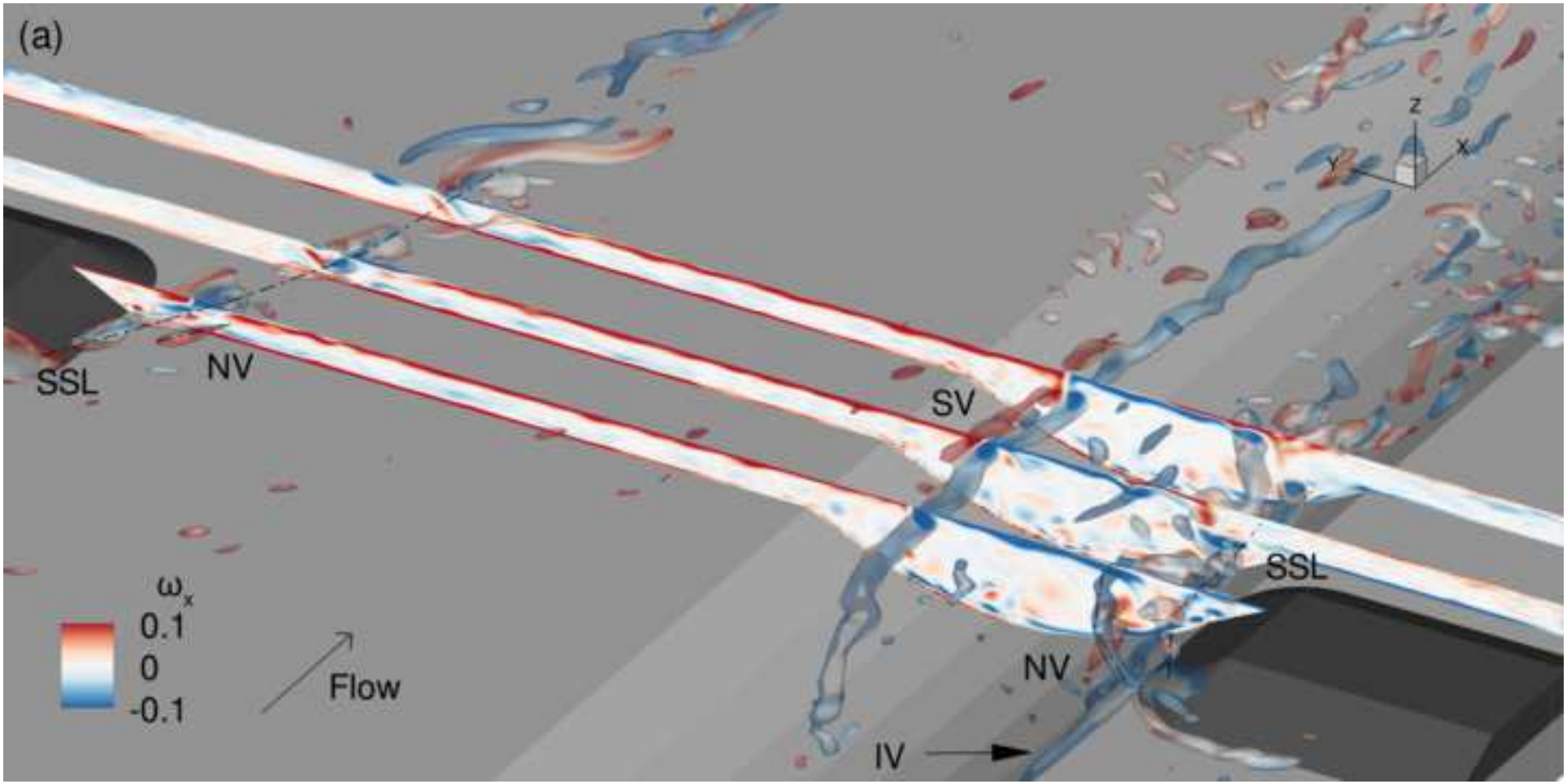

Figure 10b

Click here to access/download;Figure;fig10b.tiff

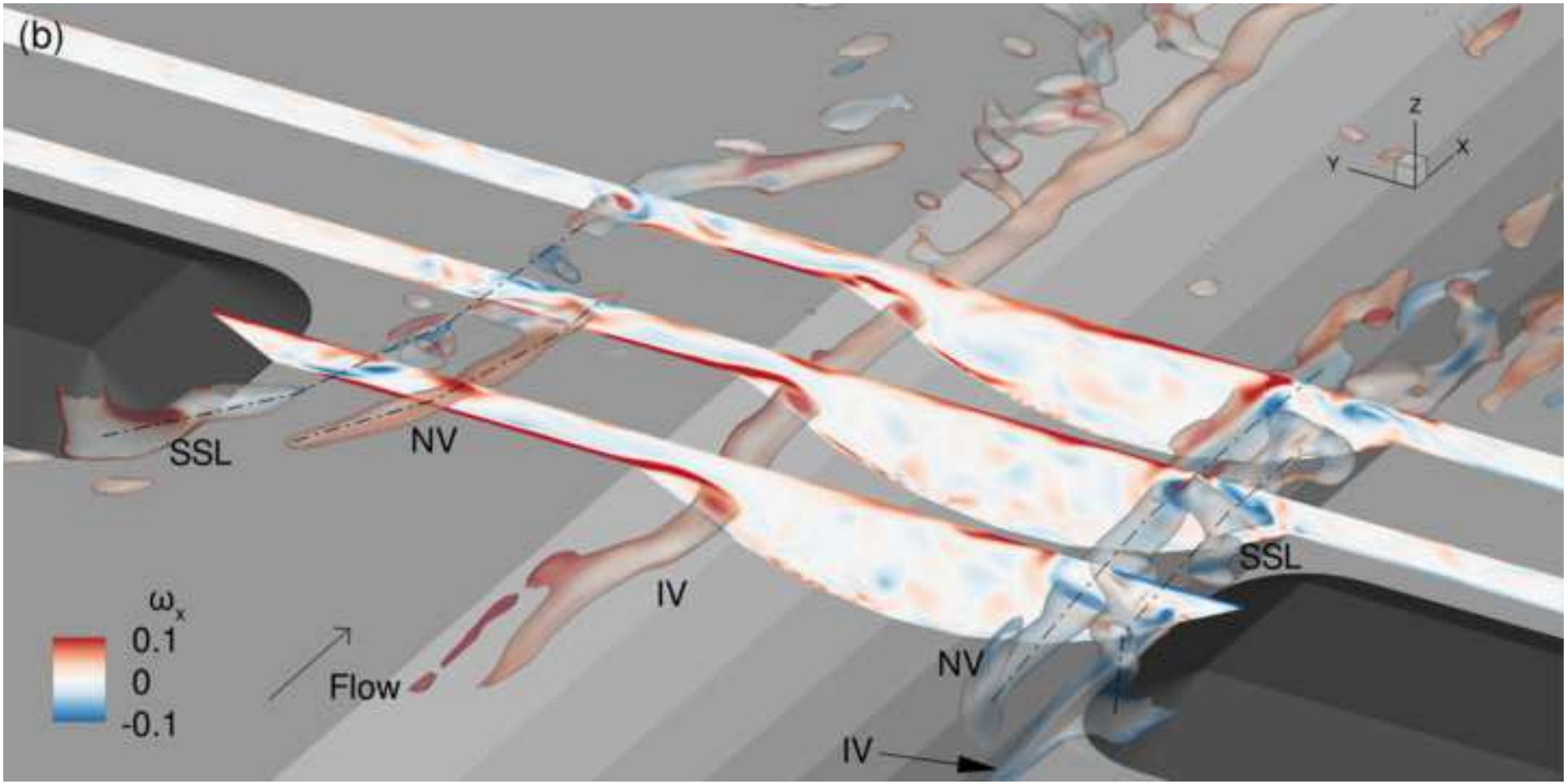

Figure 11

Click here to access/download;Figure;fig11.tiff

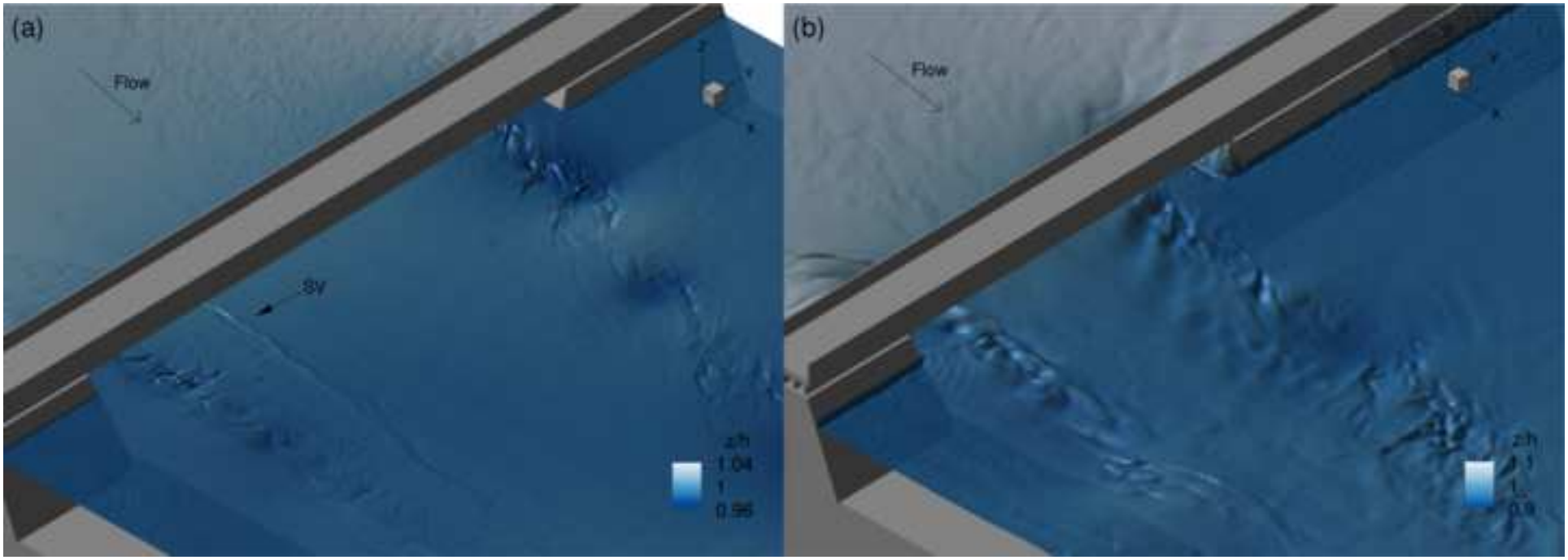

Figure 12

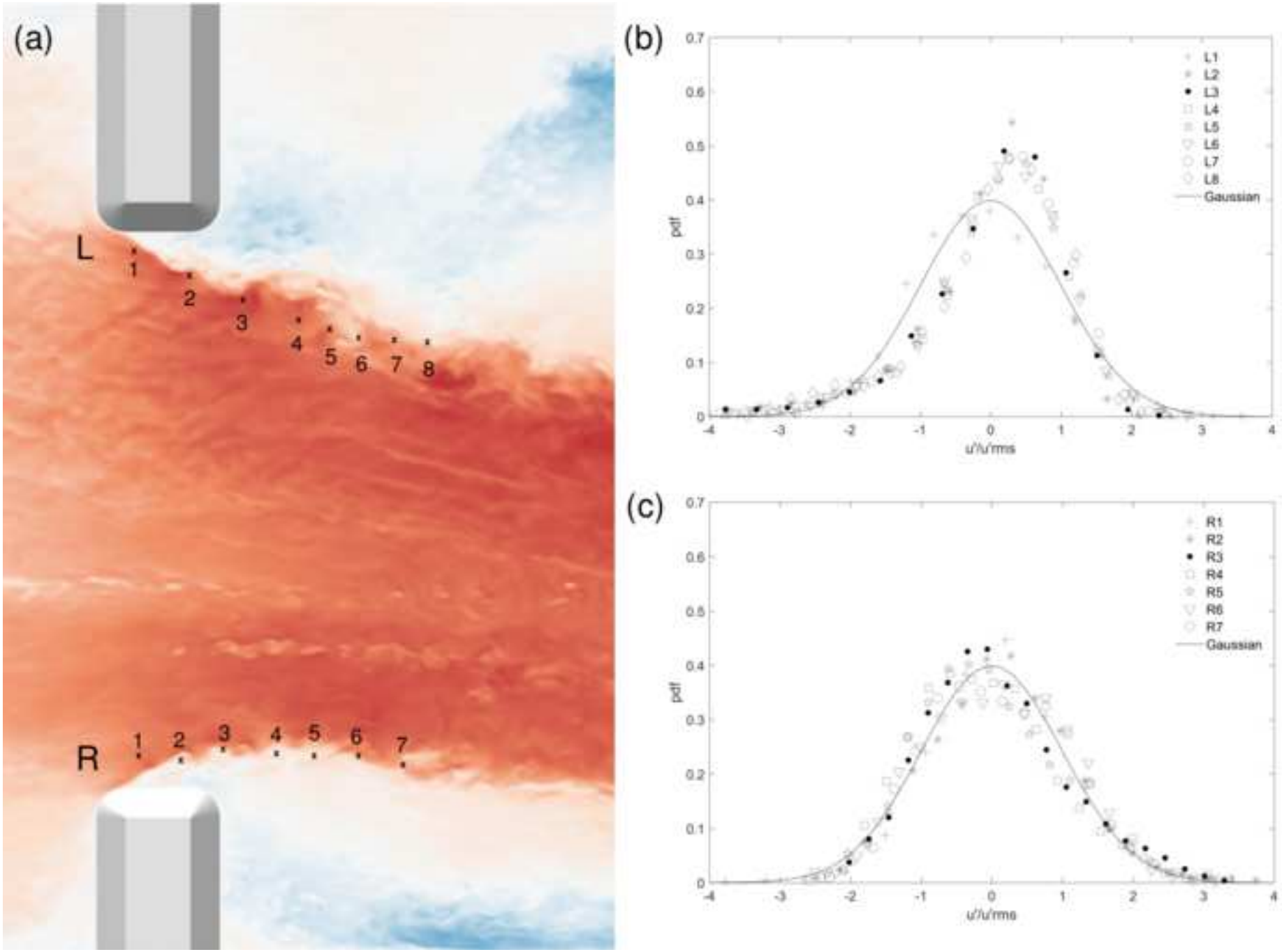

Figure 13

Click here to access/download;Figure;fig13.tiff

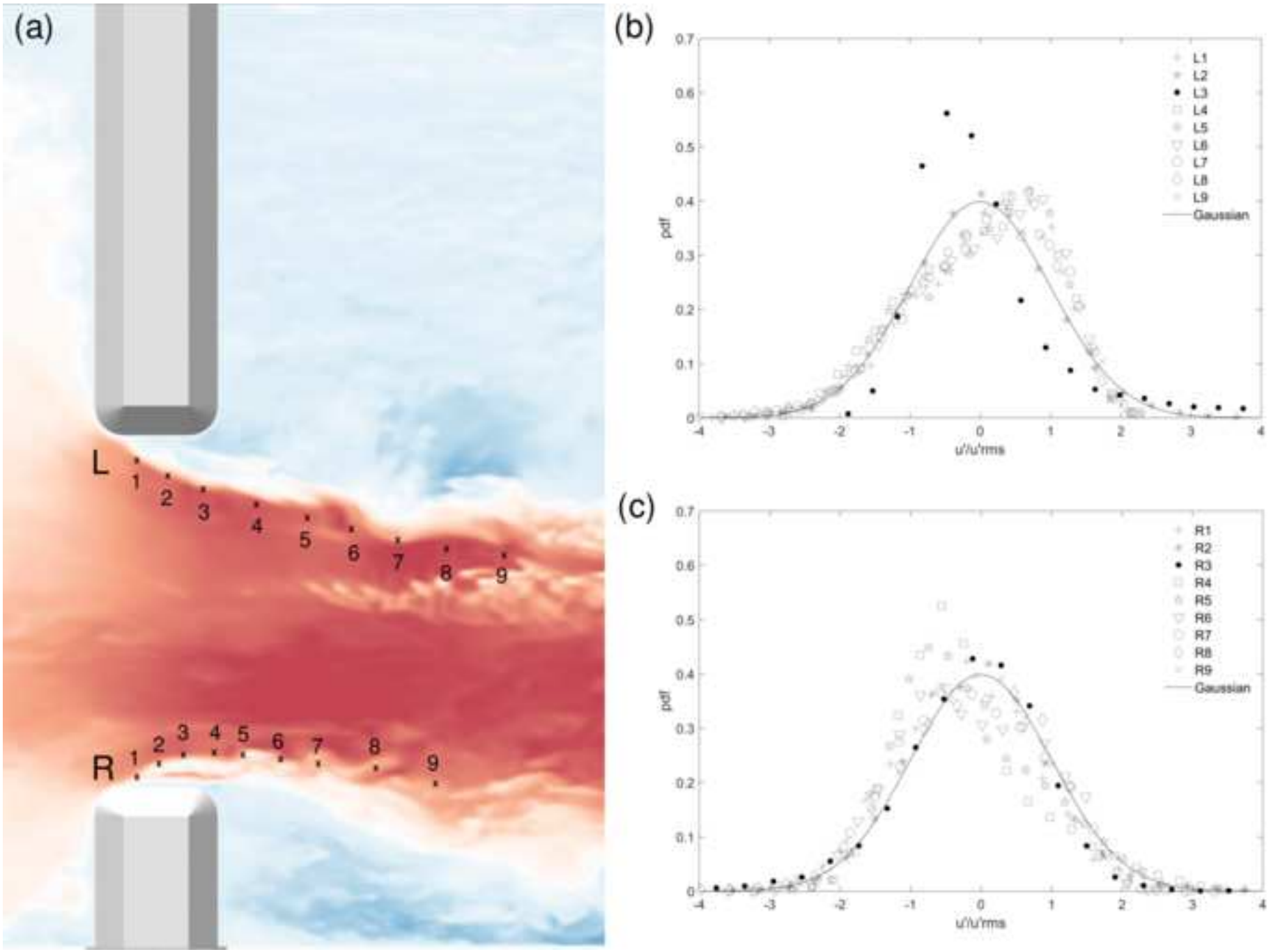

Figure 14

Click here to access/download;Figure;fig14.tiff

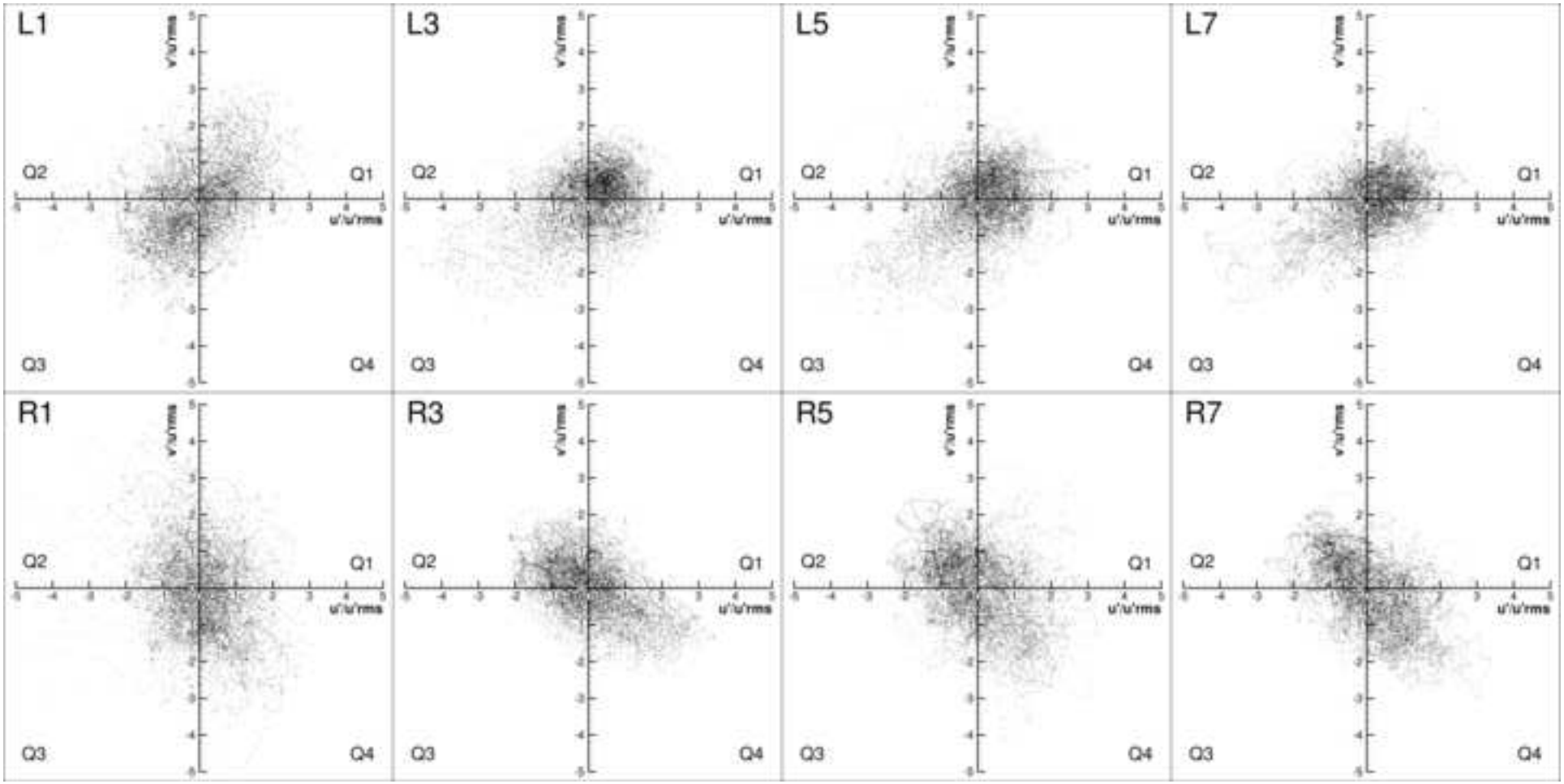

Figure 15

Click here to access/download;Figure;fig15.tiff

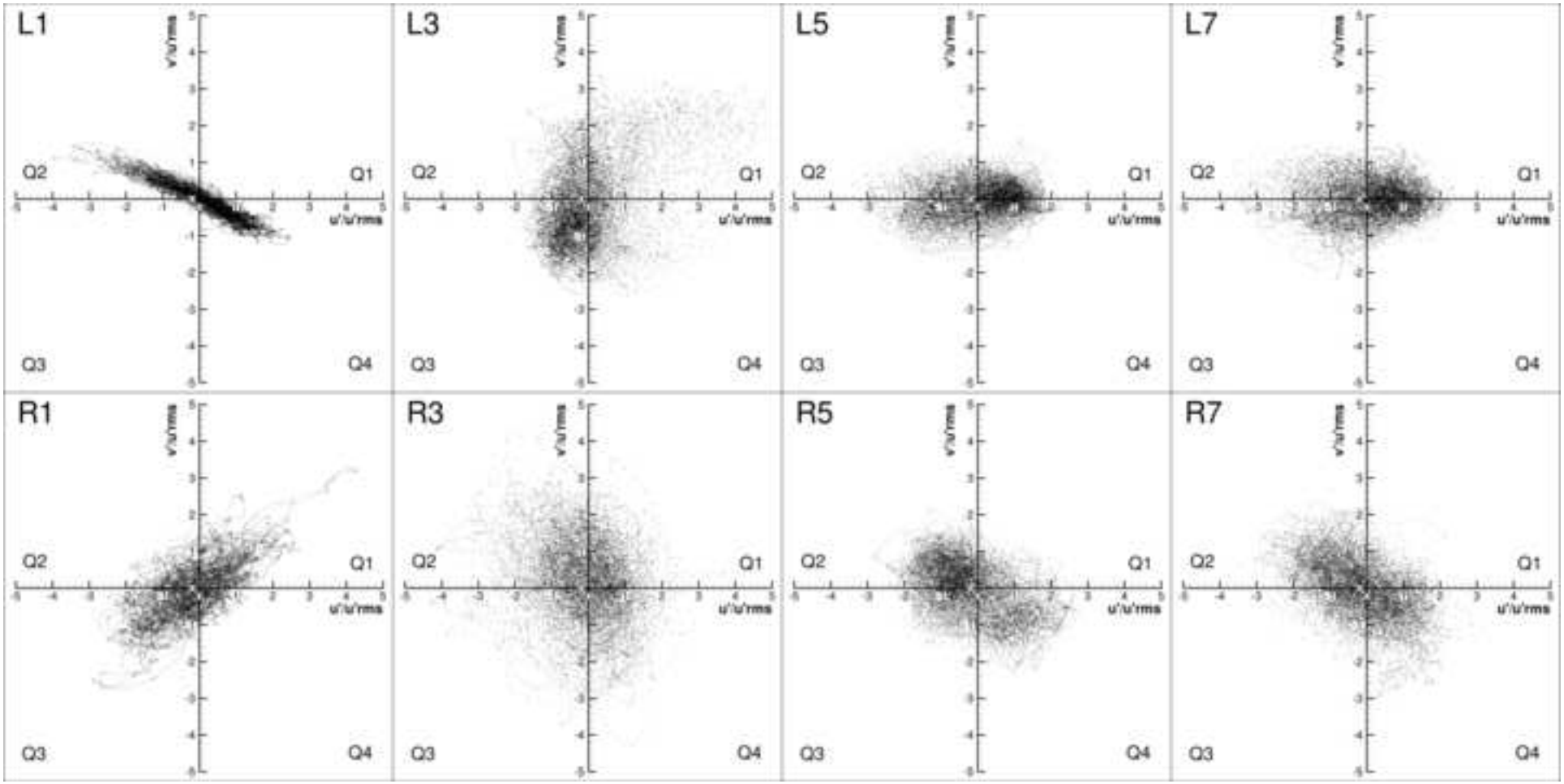

Figure 16

Click here to access/download;Figure;fig16.tiff

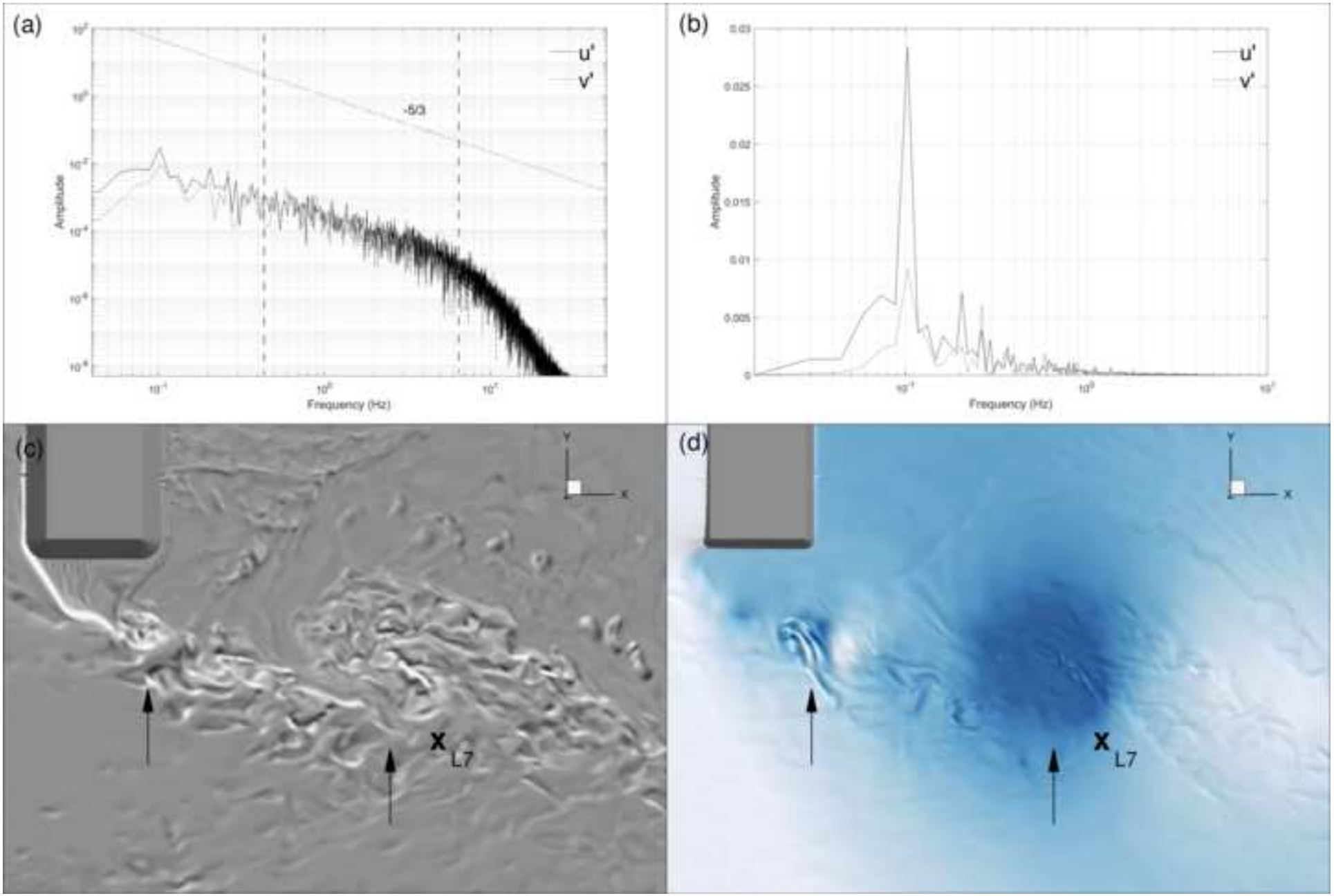

Figure 17

Click here to access/download;Figure;fig17.tiff

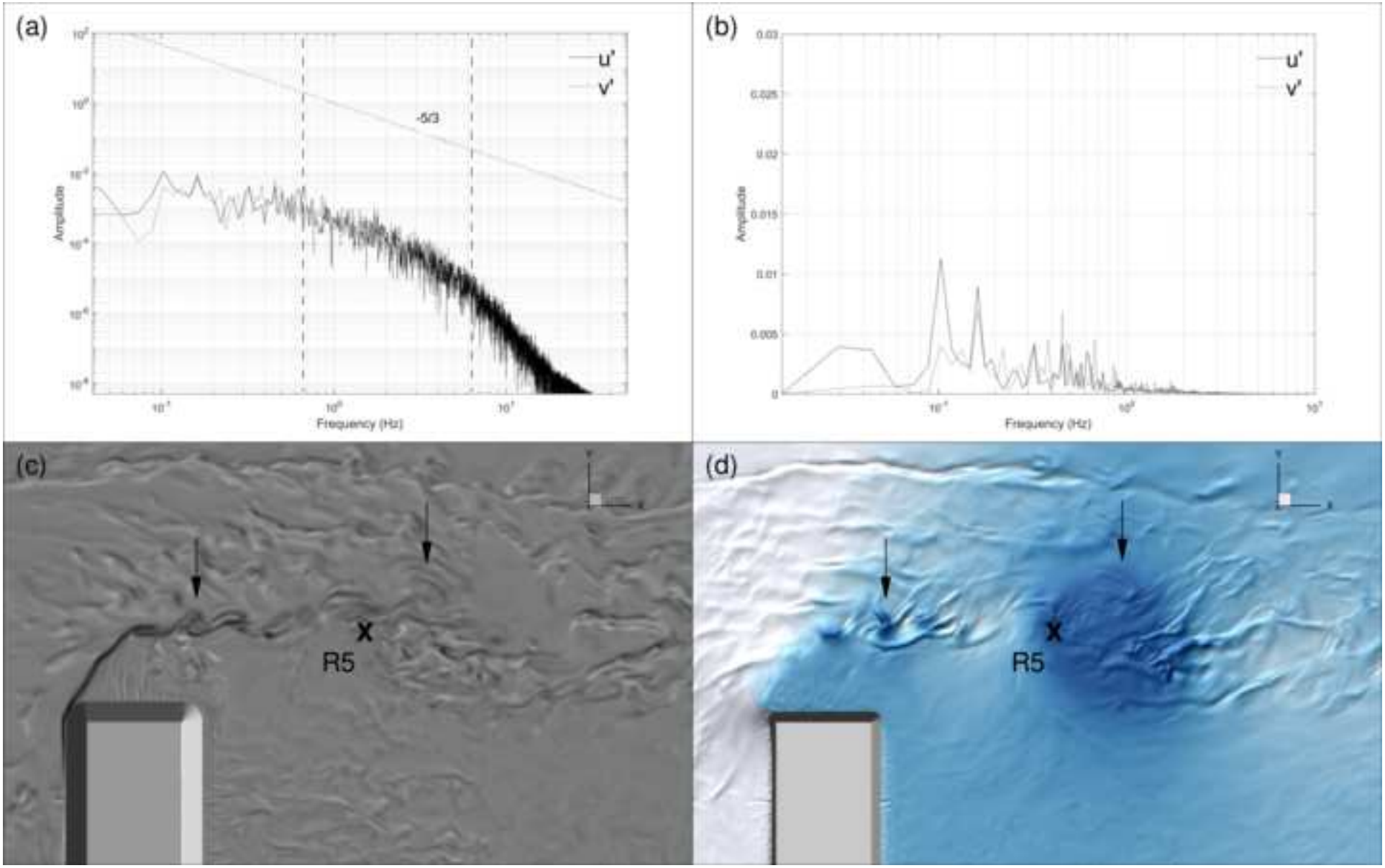

Figure 18

Click here to access/download;Figure;fig18.tiff

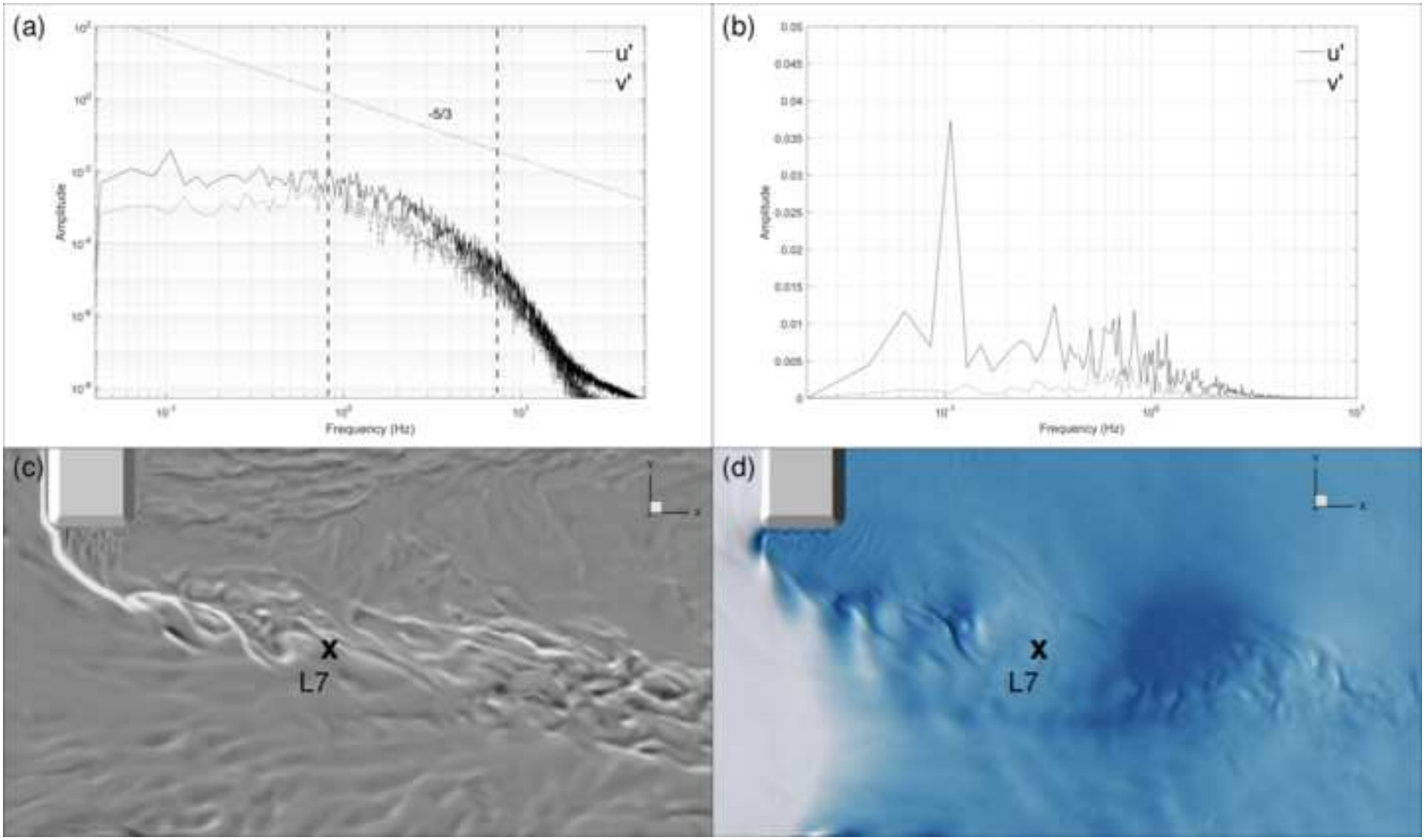

Figure 19

Click here to access/download;Figure;fig19.tiff

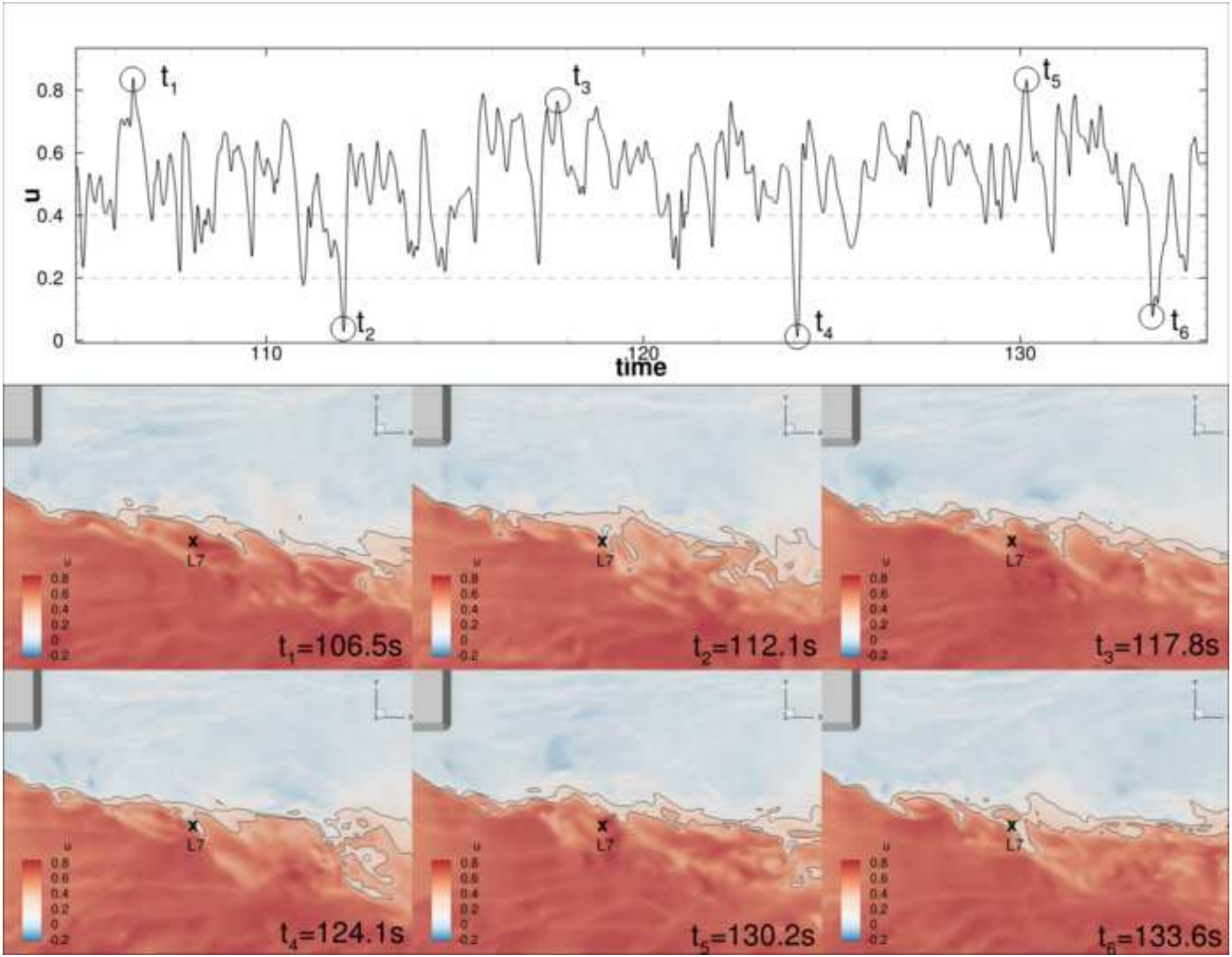

Figure 20

Click here to access/download;Figure;fig20.tiff